DERIVATION OF THE PARALLEL PIC/MCC NUMERICAL CODE AND ITS APPLICATION TO THE KINETIC ANALYSIS OF PHOTORESONANCE PLASMA AND THE PROBLEM OF IDENTIFICATION OF IMPURITIES WITHIN THE PLES METHOD

A THESIS SUBMITTED TO
THE GRADUATE SCHOOL OF NATURAL AND APPLIED SCIENCES
OF
MIDDLE EAST TECHNICAL UNIVERSITY

BY

CEMRE KUŞOĞLU SARIKAYA

IN PARTIAL FULFILLMENT OF THE REQUIREMENTS
FOR
THE DEGREE OF DOCTOR OF PHILOSOPHY
IN
PHYSICS

AUGUST 2017

Approval of the thesis:

DERIVATION OF THE PARALLEL PIC/MCC NUMERICAL CODE AND ITS APPLICATION TO THE KINETIC ANALYSIS OF PHOTORESONANCE PLASMA AND THE PROBLEM OF IDENTIFICATION OF IMPURITIES WITHIN THE PLES METHOD

submitted by **CEMRE KUŞOĞLU SARIKAYA** in partial fulfillment of the requirements for the degree of **Doctor of Philosophy in Physics Department, Middle East Technical University** by,

Prof. Dr. Gülbin Dural Ünver _____
Dean, Graduate School of **Natural and Applied Sciences**

Prof. Dr. Altuğ Özpineci _____
Head of Department, **Physics**

Assoc. Prof. Dr. İsmail Rafatov _____
Supervisor, **Physics Department, METU**

Examining Committee Members:

Prof. Dr. Arif Demir
Physics Department, Kocaeli University _____

Assoc. Prof. Dr. İsmail Rafatov
Physics Department, METU _____

Assoc. Prof. Dr. Serhat Çakır
Physics Department, METU _____

Prof. Dr. Hakan Altan
Physics Department, METU _____

Prof. Dr. Murat Tanışlı
Physics Department, Anadolu University _____

Date: _____

I hereby declare that all information in this document has been obtained and presented in accordance with academic rules and ethical conduct. I also declare that, as required by these rules and conduct, I have fully cited and referenced all material and results that are not original to this work.

Name, Last Name: CEMRE KUŞOĞLU SARIKAYA

Signature :

ABSTRACT

DERIVATION OF THE PARALLEL PIC/MCC NUMERICAL CODE AND ITS APPLICATION TO THE KINETIC ANALYSIS OF PHOTORESONANCE PLASMA AND THE PROBLEM OF IDENTIFICATION OF IMPURITIES WITHIN THE PLES METHOD

Kuşoğlu Sarıkaya, Cemre
Ph.D., Department of Physics
Supervisor : Assoc. Prof. Dr. İsmail Rafatov

August 2017, 83 pages

1d3v Particle in Cell/Monte Carlo Collision (PIC/MCC) code for numerical simulations of gas discharge plasma was developed. The efficiency of the code was increased by its parallelization using Open MPI. In order to verify the applicability of the code, the benchmark tests were performed under the RF capacitively coupled discharge conditions. The effects of the particle weighting and the Courant number on the computed plasma properties were examined and the convergence of the numerical method with respect to these parameters was demonstrated. Next, the PIC/MCC code was applied to the analysis of formation of photoresonance plasma sustained in sodium vapor. The basic plasma parameters (such as the electron energy distribution function (EEDF), ion energy distribution function (IEDF), atomic and molecular ion and electron densities, the electric field and potential) were studied. Results of the PIC/MCC simulations were compared to those obtained from the fluid model. Simulations revealed a strong spatial nonuniformity in the electron density and the electric potential over the computational domain that provides an evidence in favour of photovoltaic conversion of light energy into electrical energy. Finally, the study was focused on the problem of detection and identification of impurities in the nonlocal plasma of gas discharge within the Plasma Electron Spectroscopy (PLES) method. PIC/MCC simulations were carried out for DC glow discharge in helium doped with

a small amount of argon. Numerical results were found to be consistent with the theoretical analysis of formation of non-local EEDF and existing experimental data, and providing useful insight into the applicability and limitations of the PLES method and optimization of its operational parameters.

Keywords: PIC/MCC, PLES, Photoresonance plasma, Glow Discharge, Alkali Metal Vapor

ÖZ

PARALEL PIC/MCC NÜMERİK KODU'NUN OLUŞTURULMASI VE FOTOREZONANS PLAZMA'NIN KİNETİK ANALİZİ İLE YABANCI MADDELERİN TESPİTİNDE KULLANILAN PLES METODU'NA UYGULANMASI

Kuşoğlu Sarıkaya, Cemre
Doktora, Fizik Bölümü
Tez Yöneticisi : Doç. Dr. İsmail Rafatov

Ağustos 2017 , 83 sayfa

1d3v PIC/MCC numerik kodu yük boşalımlı plazma simülasyonu için geliştirilmiştir. Kodun verimi, kod OpenMPI ile paralel hale getirilerek arttırılmıştır. Kodun uygulanabilirliğini doğrulamak için, RF kapasitif ışın boşalımı şartları kullanılarak, simülasyon sonuçları, yayınlanmış sonuçlarla karşılaştırılarak uyumlu olduğu ispatlanmıştır. Bir süper parçacığın içerdiği gerçek parçacık sayısının ve Courant sayısının hesaplanan plazma özelliklerine etkisi incelenmiş ve nümerik metodun bu parametrelere göre yakınsaması gösterilmiştir. Daha sonra, PIC/MCC kodu, sodyum buharında fotorezonans plazmanın oluşumunun analizi için uygulanmıştır. Temel plazma parametreleri (EEDF, IEDF, atomik ve moleküler iyon ve elektron yoğunlukları, elektrik alan ve potansiyel gibi) incelenmiştir. PIC/MCC simülasyon sonuçları akışkan modelinden elde edilen sonuçlarla karşılaştırılmıştır. Sonuçta, elektron yoğunluğu ve potansiyel profilinde düzgün olmayan bir dağılım gözlenmiştir ve bu durum fotorezonans plazmanın fotoelektrik dönüştürücü olarak kullanılabilirliğini göstermektedir. Son olarak, PIC-/MCC kodu, yabancı maddelerin tespitinde kullanılan plazma elektron spektroskopisi (PLES) metoduna uyarlanmıştır. Az miktarda argon takviye edilmiş helyum gazı için DC ışınımlı deşarj simülasyonu yapılmıştır. Nümerik sonuçların, lokal olmayan EEDF oluşumunun teorik analizi ve mevcut deneysel datalar ile uyumlu olduğu ve PLES metodunun uygulanabilirliği ve sınırlamaları ile operasyonel parametrelerinin

optimizasyonu hakkında yararlı bilgiler sağladığı gözlenmiştir.

Anahtar Kelimeler: PIC/MCC, PLES, Fotorezonans plazma, Işıltılı Deşarj, Alkali Metal Buharı

Hem annem hem babamsın,
Düşmeme izin vermez, beni hep ayakta tutarsın,
Allah'tan hiçbirşey istemeye yüzüm yok,
Bana senin gibi bir melek göndermiş, daha ne yapsın.

Hakkını asla ödeyemeyeceğim canım Anneme...

ACKNOWLEDGMENTS

I have gained a very different experience and perspective with the Ph.D. program. I offer my sincere thanks to my precious adviser, Assoc. Prof. Dr. Ismail Rafatov, who guided and supported me in the most beautiful way in this process. I see myself as the luckiest person in the world because I am his student.

I would also like to thank Prof. Dr. Anatoly Kudryavtsev for illuminating my way through his precious knowledge. It's honorable for me to be able to work with him.

I wish to thank TUBITAK ULAKBIM since the numerical calculations reported in this paper were performed at TUBITAK ULAKBIM, High Performance and Grid Computing Center (TRUBA Resources).

I would also like to thank Emrah Erden, who shared his knowledge with me when I started to work on glow discharge simulation.

I am very grateful to my roommate, Kamil Çınar, for sharing my happiness and sadness in this difficult process.

I would like to thank my dear father Reşat Kuşoğlu, my guardian angel in the sky, who died when I was 9 years old, but who gave me love for 900 years, and whom I believe he has never left me.

Thank you so much to my dear mother Mey Kuşoğlu, my guardian angel on the earth, who is both a mother and a father, who devoted her life to me.

Finally, I want to thank my dear husband Onur Sarıkaya for his understanding and support during the Ph.D. program.

TABLE OF CONTENTS

ABSTRACT v

ÖZ vii

ACKNOWLEDGMENTS x

TABLE OF CONTENTS xi

LIST OF TABLES xiv

LIST OF FIGURES xv

LIST OF ABBREVIATIONS xviii

CHAPTERS

1 INTRODUCTION 1

1.1 PIC/MCC Method 1

1.2 PLES Method 3

1.3 Photoresonance Plasma 4

1.4 The Outline 5

2 PLASMAS AND DISCHARGES 7

2.1 Plasmas 7

2.2 Gas Discharge Plasmas 8

2.3 Plasma Chemical Reactions 12

3 NUMERICAL MODELS 17

3.1 Fluid Model 18

3.2 PIC/MCC Model 21

3.3 Hybrid Model 25

4 PIC/MCC CODE 27

4.1 Charge Assignment 28

4.2 Motion of Particles 29

4.3 Collisions and Boundary Conditions 34

4.4 Validation of the PIC/MCC Code 39

4.5 Parallelization of the PIC/MCC Code 43

4.6 Conclusion 47

5 SIMULATION OF THE PHOTORESONANCE PLASMA 49

5.1 Model 50

5.2 Effect of Particle Weighting 52

5.3 Effect of the Courant Number 53

5.4 Comparison to the Fluid Model 59

5.5 Results and Discussions 60

5.6 Conclusion 61

6 SIMULATION OF THE PLES METHOD 63

6.1 Model 65

6.2 Results and Discussions 66

6.3 Conclusion 70

7 CONCLUSION 71

REFERENCES 73

CURRICULUM VITAE 81

LIST OF TABLES

TABLES

Table 2.1 The various reactions that can occur on the surface and in the gas phase. *Adopted from Ref. [47].* 15

Table 4.1 The parameters used in the PIC/MCC simulation of two stream instability [79]. 31

Table 4.2 The parameters [82] used for validation of the 1d3v PIC/MCC code. 41

Table 4.3 The parameters [82] used in the parallelization test. 44

Table 5.1 The parameters used in the PIC/MCC simulation of photoresonance plasma. 51

Table 5.2 Effect of particle weighting on the total number of super electrons, the average number of super electrons per grid cell, the Debye length, λ_D, and number of super electrons per Debye length, N_D, at the steady state. λ_D and N_D were calculated about the local maximum of the electron density, using the effective temperature T_h corresponding to high energetic electron groups. 53

Table 5.3 Effect of Courant number on the total number of super electrons, the number of super electrons per Debye length, N_D, $w_{pe}\Delta t$ and $\Delta x/\lambda_D$. λ_D, N_D and w_{pe} were calculated about the local maximum of the electron density, using the effective temperature T_h corresponding to high energetic electron groups. 58

Table 5.4 The parameters used in the fluid model of photoplasma. 59

Table 6.1 The parameters used in the PLES simulation. 66

Table 6.2 The numerical parameters obtained as a result of the PLES simulation. λ_D and N_D are calculated at the position where the maximum electron density is found. 67

LIST OF FIGURES

FIGURES

Figure 2.1 Plasma classification in the energy-density space [36]. 8

Figure 2.2 The working principle of a fluorescent lamp. *Adopted from Ref.* [45]. 10

Figure 2.3 The regions in dc glow discharges, (a) at short cathode-anode distance and/or low pressure; (b) at longer cathode-anode distance and/or higher pressure (CDS = cathode dark space; NG = negative glow; FDS = Faraday dark space; PC = positive column; AZ = anode zone). *Adopted from Ref.* [1]. 11

Figure 2.4 Schematic representation of the basic plasma processes observed in the glow discharge. *Adopted from Ref.* [1]. 13

Figure 3.1 Advantages and disadvantages of the numerical models used to describe gas discharge plasmas. *Adopted from Ref.* [54]. 17

Figure 3.2 Limitations of the numerical models used to describe gas discharge plasmas. *Adopted from Ref. [55].* 18

Figure 3.3 Algorithm of PIC/MCC model. 22

Figure 4.1 Uniform distribution of the position of 200 particles obtained by random number generator. 27

Figure 4.2 Assigning charges to the grid points. 28

Figure 4.3 The scheme of the leapfrog method. 30

Figure 4.4 The electron phase space distribution obtained at $t = 0, 2.5, 5$ and 7.5. The graphs on the left are taken from the work of Fitzpatrick [79] and the ones on the right are the results of the current study. 32

Figure 4.5 The electron phase space distribution obtained at $t = 10, 12.5, 15$ and 17.5. The graphs on the left are taken from the work of Fitzpatrick [79] and the ones on the right are the results of the current study. 33

Figure 4.6 Electron cross-sections [81] in argon gas used in the townsend discharge simulation. 36

Figure 4.7 The drift velocity (a) and the mean energy (b) profiles obtained as a result of the Townsend discharge simulation. Solid line corresponds to the result from Ref. [80]. 38

Figure 4.8 Townsend coefficient profile obtained as a result of the Townsend discharge simulation. Solid line corresponds to the result from Ref. [80]. . 39

Figure 4.9 Electron cross-sections in helium gas used in the validation of PIC/MCC code [83]. 40

Figure 4.10 Ion (a) and ion power densities (b) obtained as a result of the validation test. Solid line corresponds to the result from Ref. [82]. 42

Figure 4.11 Comparison of the ion density distribution profile with the results obtained in Ref. [82]. Dashed line corresponds to the result obtained from the current work. The curves labelled A to C obtained by Turner, Derzsi and Donko, Mussenbrock, respectively. 43

Figure 4.12 Inside view of a server in the present technology. 44

Figure 4.13 Speed up (a) and efficiency (b) graphs obtained as a result of the parallelization of the code. 46

Figure 5.1 Electron cross-sections for elastic [89], excitation and stepwise ionization (from the resonance level Na(3p)) [90] collisions in sodium. . . 52

Figure 5.2 Convergence test: number of super electrons and ions versus the time step. 54

Figure 5.3 Effect of particle weighting on (a) the Na^+ ion number density and (b) the electric potential. 55

Figure 5.4 Effect of particle weighting on (a) Na^+ ion and electron mean energies and (b) the EEDF. 56

Figure 5.5 Effect of the Courant number on (a) Na^+ ion density and (b) the electric potential. 57

Figure 5.6 Effect of the Courant number on the EEDF. 58

Figure 5.7 Na^+, Na_2^+ ion and electron number densities. The figure also includes the results obtained from the fluid model. 60

Figure 5.8 The EEDF as function of the kinetic electron energy (a) and the total electron energy (b) at different regions of the discharge volume. . . . 62

Figure 6.1 Electron energy spectra in He-Ar mixture at 11 mA discharge current, 0.9 V modulating voltage and 1 mm cathode-anode gap. *Adopted from Ref. [19].* 65

Figure 6.2 Electric field and potential profiles in the He-Ar mixture. 67

Figure 6.3 Electron and helium ion density profiles in the He-Ar mixture. . . . 68

Figure 6.4 Electron and helium ion mean energies in the He-Ar mixture. . . . 68

Figure 6.5 EEDF's in the He-Ar mixture. 69

Figure 6.6 Helium ion EDF's in the He-Ar mixture. 70

LIST OF ABBREVIATIONS

$\mathbf{v}$	Velocity [$m\,s^{-1}$]
$\mathbf{a}$	Acceleration [$m\,s^{-2}$]
$\mathbf{E}$	Electric field [$V\,m^{-1}$]
$\mathbf{B}$	Magnetic field [T]
e	Elementary charge [$1.60217662 \times 10^{-19}\,C$]
k_B	Boltzmann constant [$1.38064852 \times 10^{-23}\,J\,K^{-1}$]
L	Distance between the electrodes [m]
m	Mass of the particle [kg]
n	Density [m^{-3}]
q	Electric charge of the particle [C]
P	Collision probability
Δt	Time step size [s]
ε_0	Permittivity of free space [$8.85418782 \times 10^{-12}\,F\,m^{-1}$]
μ	Mobility coefficient [$m^2\,V^{-1}\,s^{-1}$]
D	Diffusion coefficient [$m^2\,s^{-1}$]
T	Temperature [K]
p	Pressure [Pa]
ϕ	Electric potential [V]
ν	Collision frequency [s^{-1}]
R	Uniform random number between 0-1
w	Weighting of the super particle
$\mathbf{F}$	Force [N]
ρ	Charge density [$C\,m^{-3}$]

CHAPTER 1

INTRODUCTION

Glow discharge plasma is an important research topic since it is nowadays used in many technological fields such as surface modification, plasma light sources, plasma medicine, TV displays, etc. [1]. The efficient use of glow discharges as sources of plasma for these applications depends on the ability to control the plasma properties in corresponding devices. This implies a knowledge of the dependence of the plasma properties on external factors such as the chemical composition, pressure and flow rate of the gas, geometric size of the discharge setup, characteristics of electromagnetic field delivered to the plasma, etc. Such a knowledge can be obtained from numerical modelling of the processes occurring in the plasma.

1.1 PIC/MCC Method

Mostly, fluid, kinetic/particle and hybrid methods are used in simulations of glow discharge plasma. Although the fluid model is the most time-efficient method, the most accurate choice for low-temperature glow discharge plasma simulation is the PIC/MCC method. The PIC method was first used by Buneman [2] and Dawson [3] in the late 1950s to study the motion and collisions of 100-1000 particles. In those studies, the Coulomb's law was solved separately for all particles directly. In the next decade, the particle-mesh methods were introduced to solve the Poisson equation and with this method, it was possible to simulate $\sim 10^3 - 10^4$ particles. Whereupon Dawson [4] predicted theoretically the Landau damping effect of electrostatic waves in 1964, although experimentally it had not been observed yet. This study, greatly enhanced the importance of computational plasma physics. In the 1980s, classic texts on PIC's formalization and coding were published [5,6]. However, at the same time, it

was realized that the boundaries played an important role in plasmas. Later, Lawson's study [7] on boundaries made it possible to model real plasma devices. By this time, studies to improve the PIC code have been continuing and can now be used up to 10^{10} particles in this model.

The PIC method is often used in conjunction with the Monte Carlo collision (MCC) method. In the MCC method, the collision probabilities of the particles are calculated by means of the collision cross sections and these probabilities are compared with random numbers, uniformly distributed between 0 and 1, to determine whether the collision is to take place. Collisions between neutrals and charged particles were first described by Boswell [8] with simple cross-sections. Later, more realistic differential cross-sections began to be added to the literature by Vahedi and Surendra [9].

Since the PIC/MCC method gives the same result as the solution of the Boltzmann's kinetic equation, which has the form

$$\left[\frac{\partial}{\partial t} + \mathbf{v}\nabla_r + \mathbf{a}\nabla_v\right] f(\mathbf{r}, \mathbf{v}, t) = \left(\frac{\partial f}{\partial t}\right)_{coll.}, \tag{1.1}$$

where $f(\mathbf{r}, \mathbf{v}, t)$ is the distribution function, this method can be used to study the kinetic behavior of particles. The velocities and positions of particles are investigated by the Lorentz equation of motion and the electromagnetic fields by Maxwell equations. Thus, with this method, it is possible to examine the kinetic behavior of particles with few assumptions. In the PIC/MCC code, the particles are expressed by a computer particles, each of which is usually composed of $10^5 - 10^7$ real particles. This computer particle is called super particle and it is a feature that increases the efficiency of the code. In addition, interpolating particles into grids (or cells) allows for easy calculation of electromagnetic fields. Despite all of these features, many techniques such as the ion subcycling, the null collision method, etc. [10, 11] have been developed in order to make the calculation process more efficient. Nevertheless, the most successful performance improvement was achieved by parallel computing [12–14], thanks to technological improvements in computer hardware.

As mentioned earlier, the PIC/MCC method is the suitable method to work on non-local plasmas where the temperature of the electrons is much higher than that of

heavy particles (ions, atoms, molecules). For this reason, 1d3v PIC/MCC code has been developed in the scope of the present study in order to investigate some non-local plasma applications.

1.2 PLES Method

One of the non-local plasma applications investigated in the present study is the Plasma Electron Spectroscopy Method (PLES). This method was firstly developed to study the basic plasma processes and atomic constants by examining the EEDF measured by the Langmuir probe [15, 16]. Later, using the PLES method, Kolokolov et al. proposed a new method of detecting gas impurities [17, 18]. According to this new technique, impurities are detected as a result of observing the effect of Penning electrons on the EEDF resulting from Penning ionization between Helium metastable atoms and impurity atom. The reason why the Helium gas is used as the working gas is that the excitation energy of the excited Helium is larger than the ionization energy of any other gas except for Neon. Another reason why this gas is preferred is the long lifetimes of Helium metastable atoms.

As a result of the Penning ionizations between the metastable Helium atoms and impurity atoms (A) which has the form

$$He^* + A \rightarrow He + A^+ + e_p, \tag{1.2}$$

Penning electrons (e_p) are released. According to this reaction, the energies of Penning electrons, ε_p, can be calculated as

$$\varepsilon_p = \varepsilon_{meta} - \varepsilon_{ioniz}. \tag{1.3}$$

Here, ε_{meta} is the excitation energy of the metastable Helium atoms and ε_{ioniz} is the ionization energy of the impurity A. In the non-local plasma, these Penning electrons reach the electrodes without a change in their energies. Thus, these energy values can be observed as sharp peaks in the EEDF graph. In other words, impurities can

be detected as a result of analysis of EEDF graph. Kudryavtsev et al. [19–22] performed this analysis in the EEDF which they obtained experimentally. And, they successfully identified the impurities. In order to further develop this method and to determine the optimum experimental conditions, a reliable numerical simulation is needed. However, a detailed numerical analysis of PLES has not been done until now. Since this method is directed to the analysis of the non-local plasma, the numerical model should include the solution of the kinetic Boltzmann's equation. For this reason, the developed parallel 1d3v PIC/MCC code was adapted to PLES.

1.3 Photoresonance Plasma

As another application of the non-local plasma, the photoresonance plasma, in other words photoplasma, is investigated in the present work. Photoplasma is a partially ionized gas generated by light radiation [23]. In 1930, when Mohler and Boeckner applied resonance radiation to cesium vapor, they observed the formation of ions and thus became the first observers of this phenomenon [24]. Photoplasma is generated by resonance absorption of the incident light. As a result, as in the PLES method, charged particles are formed mainly by Penning ionization.

Systematic studies on photoresonance plasma were started in 1967 by Morgulis, Korchevoi and Przhonskii, who produced high-density photoplasma by irradiating the cesium vapor with resonance radiation [25]. The ensuing investigations [26–28] enabled to learn about the mechanisms and rate of processes involving excited atoms. Photoplasma provides advantages in many applications such as in the charge-transfer collision cross-section measurements, the production of isotopically pure elements, the purification of alloy, etc. [23]. In addition, it has also been observed to be advantageous in experiments on conversion of laser energy to electrical energy. For example, Brandenberger [29] illuminated Krypton gas perpendicularly to its axis by laser light with a wavelength of 785.5 nm (1s3 $\rightarrow$ 2p3 transition) and observed a photo emf in the microwave discharge in Krypton. About 0.1 V potential difference was obtained at a laser power of about 1 mW. This potential difference was caused by inhomogeneity of light induced changes of the Kr metastable (1s3) density. Also, recently, Gorbunov and Stacewicz [30, 31] used the ambipolar potential difference

method in their experiments to analyze the direct conversion of the kinetic energy of charged plasma particles into electric current by using the laser light. As a result of these experiments, the photo-emf was obtained as high as 3-4 V, which was almost one order of magnitude higher than that for semiconductor converters.

The possibility of using photoplasma to convert solar energy into electric energy [32] is potentially promising. As known, the most important requirement of all energy converters is that the energy flux density of sunlight must be high for an effective conversion. In order for solar radiation to provide this high density, lenses or mirrors are needed. Solar light concentration can be increased $10 - 1000$ times with these apparatuses and a certain increase in the efficiency of semiconductor converters can be reached [33]. However, in this case, there is a problem of superheating. Whereas, it is possible to reach high temperatures by using photoplasma as a photoelectric converter. In addition, plasma converters have many advantages. First, a more efficient charge separation in plasma can lead to a more efficient conversion. Second, the presence of a wide absorption spectrum of the plasma allows to utilize all of the energy of sunlight.

Dunning and Palmer [34] performed the first experiment for this plasma converters based on the MHD generators. They created the photoplasma by heating cesium vapor with concentrated solar radiation using a heat pipe. However, as much as the experiments, the theoretical investigations [34,35] on this subject is also rather limited and a numerical analysis has not been done yet using a kinetic approach. Therefore, in order to understand the underlying physics of this subject in detail, 1d3v parallel PIC/MCC simulation of photoplasma in sodium alkali metal vapor exposed to light radiation was performed in the present work.

1.4 The Outline

In Chapter 2, gas discharge plasmas are described and possible chemical reactions that may occur in these plasmas are summarized. Because of the significant technological improvements in computer hardware, plasma simulation methods play an effective role in the development of this topic. The detailed description of these methods and

their advantages and disadvantages are within the scope of Chapter 3. In Chapter 4, firstly, the techniques used in the development of this code are explained step by step. Later, the benchmark study to demonstrate the reliability of the code, and the parallelization of the code to provide increased performance, are also discussed in this Chapter. Parallel 1d3v PIC/MCC code was firstly adapted to photoresonance plasma simulation in sodium alkali metal vapor exposed to light radiation. The methods used in this simulation and the results are explained in detail in Chapter 5. The code was also used to simulate PLES method in order to identify the impurities in helium gas. The simulation model is described and the results of this simulation are analyzed in Chapter 6. Finally, in Chapter 7, the results of the PLES simulation and the usability of photoplasma as a photoelectric converter are discussed.

CHAPTER 2

PLASMAS AND DISCHARGES

2.1 Plasmas

Plasma is usually considered as the fourth state of matter along with solids, liquids and gases. It represents an ionized gas and consists of almost equal numbers of positive and negative charges. It is known that the vast majority of our visible universe is plasma. Plasmas can be divided into those that are in thermal equilibrium and those that are not in thermal equilibrium. Thermal equilibrium means that the temperature of all particles (electrons, ions and neutrals) is the same. High temperature is needed for this equilibrium to happen. This can be seen, for example, in stars and in fusion plasmas. However, in non-thermal equilibrium, the plasma particles do not have the same temperature. In such cases, the temperature of the electrons is much higher than that of the heavy particles (ions, atoms, molecules).

Plasmas are usually classified according to the density of the charged particles and the thermal energies of the electrons. As can be seen in Fig. 2.1, there are too many different type of plasmas even in a small region of the density-energy parameter space.

Plasmas can be formed in laboratories. The local thermal equilibrium (LTE) term, which defines the thermal equilibrium in localized areas in the plasma, is often used in order to classify the gas discharge plasmas. This term is related to the gas pressure. A high gas pressure ($10 - 10^3$ kPa) causes too many collisions (i.e. a short collision mean free path) and thus an efficient energy exchange between the particles. This exchange gives rise to the particles to have equal temperatures. This type of gas discharge is called as LTE plasmas. As opposed to this, a low gas pressure ($10^{-4} - 1$ kPa) causes a few collisions and thus the particles have different temperatures as a

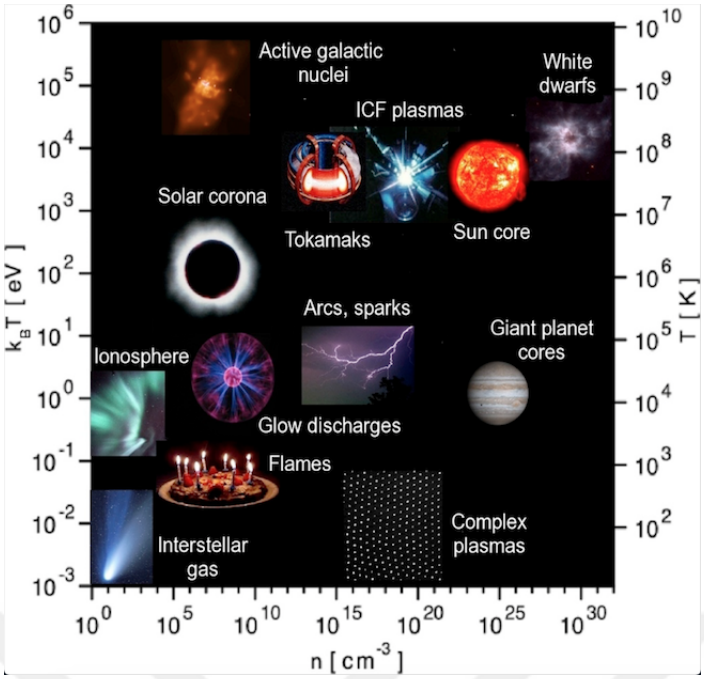


Figure 2.1: Plasma classification in the energy-density space [36].

result of inefficient energy exchange. Such a gas discharge is defined as non-LTE which is the scope of this thesis.

2.2 Gas Discharge Plasmas

Sources such as electric current or electromagnetic radiation are needed to create laboratory gas discharge. There are many types of these sources such as direct current (dc), capacitively coupled radiofrequency (rf), inductively coupled rf and microwaves [1, 37]. With these sources, energy is transferred to the electron and as a result, electrons start drifting with drift velocity,

$$\mathbf{v_d} = -\mu \mathbf{E}, \tag{2.1}$$

which is proportional to the electric field (E) and as a result the electron current

density is defined as

$$\mathbf{j} = ne\mathbf{v_d}, \tag{2.2}$$

where μ is the electron mobility. Then, electrons cause ionization to form charged particles by colliding with neutrals in the discharge plasma region. In this way, charged particles are created within the physical boundaries. With the formation of charged particles, the potential begins to shape at the sheath region where it changes rapidly. The length of this region is called the Debye length, λ_D, and has the form

$$\lambda_D = \sqrt{\frac{\varepsilon_0 k_B T_e}{n_e e^2}}. \tag{2.3}$$

Here, T_e and n_e denote the electron temperature and density, k_B is the Boltzmann constant and ε_0 is the vacuum permittivity. In the plasma region, the potential changes much more slowly. When the Poisson equation,

$$\frac{d^2\phi}{dx^2} = \frac{(n_e - n_i)e}{\varepsilon_0}, \tag{2.4}$$

is rewritten as

$$\frac{\phi}{l^2} \approx \frac{(n_e - n_i)e}{\varepsilon_0}, \tag{2.5}$$

it can be seen that in the case of $n_i \sim n_e$, the potential changes only at large distances. Where the electrons leave the quasineutral region faster than ions, positive space charge forms and the potential starts to fall.

In general, it is possible to observe the transformation of particles, momentum or energy in the plasmas. Each of these transformations allowed the use of laboratory plasmas in various technological applications. For example, while the transformation of particles is used in areas such as surface modification or powder formation [37,38], ozone generation and environmental applications [39,40], momentum transformation is beneficial in plasma thrusters and rocket propulsion [41]. The transformation of

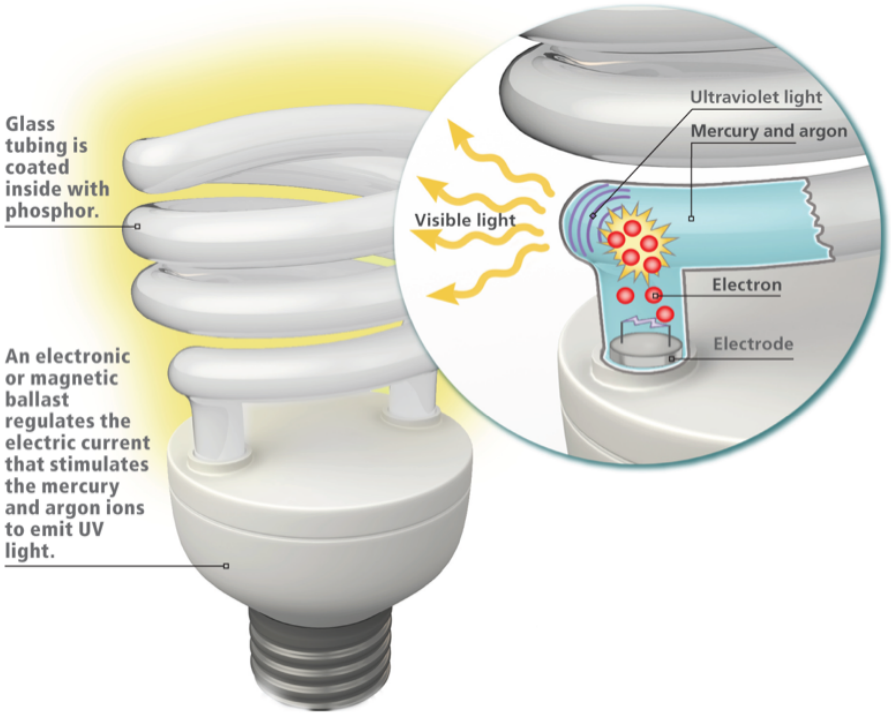


Figure 2.2: The working principle of a fluorescent lamp. *Adopted from Ref.* [45].

energy, on the other hand, is used efficiently in light production such as in lamps [42], plasma displays [43] or lasers [44].

The oldest application of gas discharge are the fluorescent lamps (see Fig. 2.2). Fluorescent lamps are low-pressure non-LTE plasma lamps. The electrodes in the bulb are made of materials with a high electron emission coefficient in order to feed the discharge with sufficient electrons. The potential difference applied to the electrodes causes the electrons to accelerate and collide with the mercury atoms and excite them as seen in Fig. 2.2. As a result of this excitation, the UV radiation is absorbed by the fluorescent layer and converted into visible light. Detailed information about other applications of gas discharge and the resources used to create the laboratory plasmas, have been recently reviewed in Ref. [1, 37].

In this work, we will typically concentrate on glow discharge plasmas. Parameters characterizing these type of discharges are in general functions of "pressure times the discharge gap", pL [46]. Typical anatomy of the glow discharges is demonstrated in Fig. 2.3, two different potential (the solid) and electric field (the dashed) distribu-

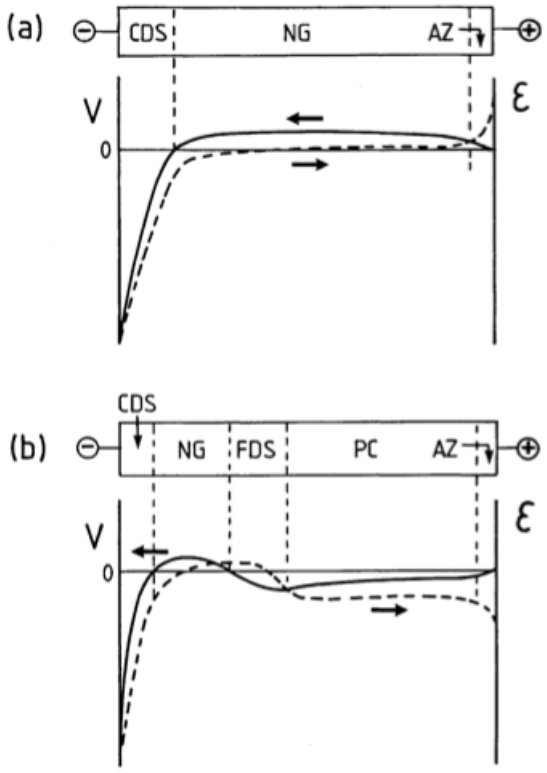


Figure 2.3: The regions in dc glow discharges, (a) at short cathode-anode distance and/or low pressure; (b) at longer cathode-anode distance and/or higher pressure (CDS = cathode dark space; NG = negative glow; FDS = Faraday dark space; PC = positive column; AZ = anode zone). *Adopted from Ref.* [1].

tions obtained for dc glow discharge are shown. While Fig. 2.3a was obtained for a short cathode-anode distance (and/or low pressure), the second one was obtained for a longer interelectrode distance (and/or higher pressure). As can be seen, in the first region, the voltage drops almost to zero. This region corresponds to a strong electric field and is called the 'cathode dark space (CDS)' or 'sheath'. The region where the potential is almost constant is the largest part of the discharge (Fig. 2.3a) and is called 'negative glow (NG)'. But it is also called the 'plasma potential'. Finally, the short zone where the potential returns to zero from this region is called the 'anode zone (AZ)'.

When the distance between electrodes is longer, as in Fig. 2.3b, the 'Faraday dark space (FDS)' and the 'positive column' regions can be seen. In these regions, negative electric field directs the electrons toward the anode. These zones are often found in

lasers and fluorescence lamps. However, in other dc applications these regions are not encountered since the interelectrode distance is generally short in these applications.

2.3 Plasma Chemical Reactions

It is known that an external electric field applies force to each charged particle in the plasma. With the work done by this force, the particles gain energy. This energy causes the particles to interact with each other in various ways. Momentum and energy conservation are essential during these interactions. Taking into account these conservations, the particles can perform many reactions.

The various reactions that can occur in plasma are summarized in Table 2.1. There is a certain probability that it is possible to determine whether each of these reactions will occur. This probability is called a collision cross-section and is indicated by σ. When we look at this value of each process that possible to occur, it is seen that some of the reactions have much more importance in the glow discharge plasma (see Fig. 2.4). The most dominant among these important reactions are the reactions involving electrons. Electrons can basically perform collisions in three different ways: elastic, inelastic and super elastic.

Elastic collision can be considered as distribution of the total momentum to the particles in a different way,

$$e^- + A \rightarrow A + e^-. \tag{2.6}$$

This reaction has the role of limiting the velocity of the electrons in the direction of the electric field. During this type of collision, the total kinetic energy is also conserved.

All of the remaining collisions of electrons are called inelastic. In this case, the kinetic energy is not conserved and a certain amount of this energy is turned into the internal

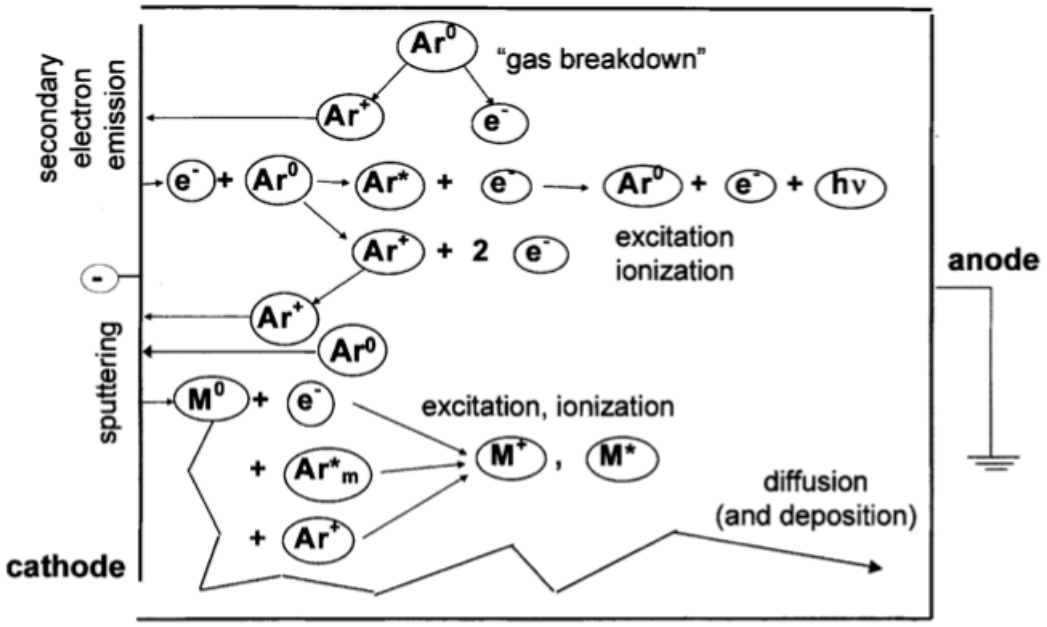


Figure 2.4: Schematic representation of the basic plasma processes observed in the glow discharge. *Adopted from Ref.* [1].

energy of particle. The first example of this collision type is the ionization,

$$e^- + A \rightarrow A^+ + e^- + e^-, \tag{2.7}$$

which enables to obtain sustainable glow discharge. With this collision, the electron, if its energy is greater than the ionization threshold, removes an electron from the atom, resulting in two electrons and a positive ion. Ionization threshold is the energy which is required to remove the weakest electron bounded to the atom. Two electrons that form as a result of ionization are accelerated by the electric field and then perform the same ionization event separately. So that the number of ions and electrons multiplies and prevent the glow discharge from being extinguished.

Electron impacts can also cause bound electrons to jump to higher energy levels. This jump is called excitation,

$$e^- + A \rightarrow A^* + e^-, \tag{2.8}$$

and again requires a minimum energy, called the excitation threshold, to be realized. The process opposite to excitation is called relaxation,

$$e^- + A^* \rightarrow e^- + A + h\nu \tag{2.9}$$

and as a result of this relaxation, photons corresponding to the energy difference between energy levels are emitted. This is the reason why there is glow in a glow discharge.

Besides the electrons, the ions can also collide with the neutrals at a considerable degree in the glow discharge. The most important of these are elastic collisions as electrons do, and charge exchange collisions,

$$A^+ + B \rightarrow B^+ + A. \tag{2.10}$$

With charge exchange, the neutrals are converted to ions and the ions to neutrals. The effect of this reaction can be observed in the energy distributions of ions and neutrals.

The collision of an excited atom with the neutral becomes important when the excitation energy of the excited atom is greater than the ionization threshold of the neutral. In this case, the neutral becomes ionized and an electron is released. Such a reaction is called Penning ionization,

$$A + B^* \rightarrow A^+ + B + e^-, \tag{2.11}$$

and the electron formed as a result of this reaction is called penning electron.

Finally, as the particles collide with each other, they can also make some reactions at the boundaries. For example, accelerated positive ions through the electric field can hit the negative electrode and cause an electron to emit from the electrode,

$$A^+(fast) \rightarrow A + e^-. \tag{2.12}$$

These electrons are called secondary electrons. The probability of formation of secondary electrons, which is defined by the secondary electron emission coefficient (γ), varies according to the electrode type. Furthermore, the particles may be reflected back from the electrodes, and the probability of this reflection, which is defined by the reflection coefficient (r), depends also on the electrode type.

Table 2.1: The various reactions that can occur on the surface and in the gas phase. *Adopted from Ref. [47].*

Reactions	Description	Evidence
Surface reactions		
$AB+C_{solid} \rightarrow A+BC_{vapour}$	etching	material erosion
$AB \rightarrow A + B_{solid}$	deposition	thin film formation
$e^- + A^+ \rightarrow A$	recombination	major loss process
$A^* \rightarrow A$	de-excitation	
$A^* \rightarrow A + e^-$	secondary emission	Auger electrons
$A^+(fast) \rightarrow A + e^-$	secondary emission	Auger electrons
Gas phase reactions involving electrons		
$e^- + A \rightarrow A + e^-$	elastic scattering	thermal electrons
$e^- + A \rightarrow A^+ + e^- + e^-$	ionization	conductivity
$e^- + A \rightarrow A^* + e^-$	excitation	
$e^- + A^* \rightarrow e^- + A + h\nu$	de-excitation	light emission
$e^- + A^* \rightarrow A^+ + e^- + e^-$	two step ionization	ionization efficiency
$e^- + AB \rightarrow A + B + e^-$	fragmentation	residual gas analysis
$e^-+AB \rightarrow A^+ + e^- + B + e^-$	dissociative ionization	
$e^- + AB \rightarrow A^- + B$	dissociative attachment	
$e^- + A^+ + B \rightarrow A + B$	volume recombination	plasma decay and steady-state
Gas phase reactions involving ions and neutrals		
$A^+ + B \rightarrow B^+ + A$	charge exchange	ion energy spectra
$A^+ + B \rightarrow B + A^+$	elastic scattering	ion energy spectra
$A^+ + B \rightarrow A^+ + B^* + e^-$	excitation	ionization efficiency
$A^+ + B \rightarrow A^+ + B^+ + e^-$	ionization	ionization efficiency
$A + B^* \rightarrow A^+ + B + e^-$	Penning ionization	ionization efficiency
$A^+ + BC \rightarrow A^+ + B + C$	fragmentation/dissociation	residual gas analysis
$e^- + A^+ + B \rightarrow A + B$	volume recombination	plasma decay
$A^\pm + B \rightarrow AB^\pm$	oligomerization	ion mass spectra
$A + B \rightarrow AB$	oligomerization	residual gas analysis

CHAPTER 3

NUMERICAL MODELS

A reliable simulation provides convenience in many ways. In addition to providing a better understanding of problems in the field of research, it is very useful in determining the optimum parameters to be used in experiments and determining the conditions required for performance improvement. There are many different models used to describe gas discharge plasmas, such as analytical models [48], fluid modeling [49], the Boltzmann transport equation [50], Monte Carlo [51], particle-in-cell simulations [52] and hybrid models [53]. Each of these models has advantages and disadvantages which are summarized in Fig. 3.1.

Model	Short description	Advantage	Disadvantage
Analytical	Simple equations	Simple, fast	Approximation
Fluid	Momentum equations of Boltzmann equation	Simple, fast, self-consistent	Approximation (thermal equilibrium)
Boltzmann	Full Boltzmann equation	Nonequilibrium	Complex
Monte Carlo	Newton's laws + random numbers	Accurate	Long calculation time, not self-consistent
Particle-in-cell	As above + Poisson equation	Accurate + self-consistent	Long calculation time
Hybrid	Combination of above models	Accurate + self-consistent, reduced calculation time	—

Figure 3.1: Advantages and disadvantages of the numerical models used to describe gas discharge plasmas. *Adopted from Ref.* [54].

The limits of PIC/MCC, fluid and hybrid models on the pressure-length scale are

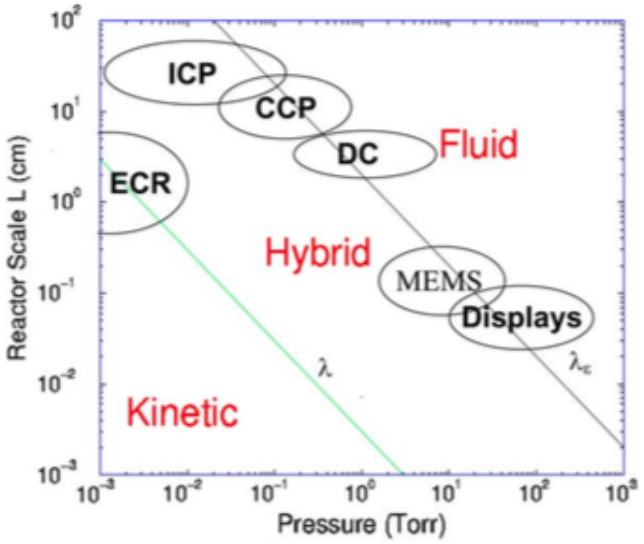


Figure 3.2: Limitations of the numerical models used to describe gas discharge plasmas. *Adopted from Ref. [55].*

shown in Fig. 3.2. The fluid model is based on the moments of the Boltzmann equation (Eq. (1.1)). Despite being a simple and fast, it fails to describe non-local plasma behaviour due to the assumptions it contains. Such a plasma can be simulated using the solution of the Boltzmann equation. However, since this solution is extremely complicated mathematically, the PIC/MCC method can be used as an alternative to this method. The disadvantage of the PIC/MCC model in terms of time consumptions increases the importance of the hybrid models. The hybrid model can be formed by combining different models according to the physics to be investigated. Thus, the advantages of different models can be achieved within one model.

3.1 Fluid Model

The fluid model is used to describe plasma with macroscopic quantities such as particle, momentum and energy densities. In order to calculate these quantities, the continuity, the momentum and the energy equations obtained from the Boltzmann equation [56, 57] need to be solved.

The continuity equation,

$$\frac{\partial n}{\partial t} + \nabla \cdot (\mathbf{v}n) = 0, \tag{3.1}$$

is obtained from the zeroth moment of the Boltzmann equation (Eq. (1.1)). The first moment correspond to the momentum equation,

$$mn\frac{d\mathbf{v}}{dt} = qn\left(\mathbf{E} + \mathbf{v} \times \mathbf{B}\right) - \nabla \cdot p + \nu. \tag{3.2}$$

Finally, the energy balance equation is obtained from the second moment as

$$\frac{3}{2}n\frac{dkT}{dt} + p\nabla \cdot \mathbf{v} = 0. \tag{3.3}$$

These equations are written for the electrons as

$$\frac{\partial n_e}{\partial t} + \nabla \cdot (\mathbf{v_e}n_e) = S_e, \tag{3.4}$$

$$m_e n_e \frac{d\mathbf{v_e}}{dt} = q_e n_e \left(\mathbf{E} + \mathbf{v_e} \times \mathbf{B}\right) - \nabla \cdot p_e - \nu_{en} m_e n_e \left(\mathbf{v_e} - \mathbf{v_n}\right) - \nu_{ei} m_e n_e \left(\mathbf{v_e} - \mathbf{v_i}\right), \tag{3.5}$$

$$\frac{3}{2}n_e\frac{dkT_e}{dt} + p_e\nabla \cdot \mathbf{v_e} = Q_{ei}, \tag{3.6}$$

and for the ions as

$$\frac{\partial n_i}{\partial t} + \nabla \cdot (\mathbf{v_i}n_i) = S_i, \tag{3.7}$$

$$m_i n_i \frac{d\mathbf{v_i}}{dt} = q_i n_i \left(\mathbf{E} + \mathbf{v_i} \times \mathbf{B}\right) - \nabla \cdot p_i - \nu_{ie} m_i n_i \left(\mathbf{v_i} - \mathbf{v_e}\right) - \nu_{in} m_e n_e \left(\mathbf{v_i} - \mathbf{v_n}\right), \tag{3.8}$$

$$\frac{3}{2}n_i\frac{dkT_i}{dt} + p_i\nabla\cdot\mathbf{v_i} = Q_{ie}. \tag{3.9}$$

where S is the source function and Q is the energy exchange rate between the plasma species.

Considering $m_e \ll m_i$, $\mathbf{v_e} \gg \mathbf{v_n}, \mathbf{v_i}$ and $p_e = n_e kT_e$, the momentum equation for the electrons become the form

$$n_e\mathbf{v_e} = -D_e\nabla\cdot n_e - \mu_e n_e\mathbf{E} - \mu_e n_e\left(\mathbf{v_e}\times\mathbf{B}\right). \tag{3.10}$$

Similarly, by assuming

$$\nu_{ie}m_i n_i\left(\mathbf{v_i}-\mathbf{v_e}\right) = -\nu_{ei}m_e n_e\left(\mathbf{v_e}-\mathbf{v_i}\right) \tag{3.11}$$

with $\mathbf{v_n} = 0$ and $m_e\nu_{en} \ll m_i\nu_{in}$, the momentum equation for the electrons will have the form

$$n_i\mathbf{v_i} = -D_i\nabla\cdot n_i - \mu_i n_i\mathbf{E} - \mu_i n_i\left(\mathbf{v_i}\times\mathbf{B}\right). \tag{3.12}$$

By putting these results into the continuity equations (Eqs. 3.4 and 3.7), the fluid equations with drift-diffusion approximation are obtained as [58, 59]

$$\frac{\partial n_e}{\partial t} + \nabla\cdot\left(-\mu_e n_e\mathbf{E} - D_e\nabla\cdot n_e\right) = S_e, \tag{3.13}$$

$$\frac{\partial n_i}{\partial t} + \nabla\cdot\left(\mu_i n_i\mathbf{E} - D_i\nabla\cdot n_i\right) = S_i, \tag{3.14}$$

where the total electron and ion flux densities have the form

$$\mathbf{\Gamma_e} = -\mu_e n_e\mathbf{E} - D_e\nabla\cdot n_e, \tag{3.15}$$

$$\mathbf{\Gamma_i} = -\mu_i n_i \mathbf{E} - D_i \nabla \cdot n_i. \tag{3.16}$$

Besides these equations, finally, the Poisson equation which has the form

$$\nabla \cdot (\varepsilon \nabla \phi) = -e(Z_i n_i - n_e), \tag{3.17}$$

is solved to obtain the potential distribution corresponding to the spatial distribution of the particles. Commonly used methods of numerical solution of fluid equations of plasma are finite difference, finite volume, and finite element methods [5, 60].

The most important advantage of the fluid model is the speed of calculation. With this model, even three-dimensional simulations can be completed in a relatively short time. On the other hand, the assumptions used prevent the study of the kinetics of non-local particles. In general, the fluid model is insufficient to account for non-local plasma discharges where the electron mean free path is greater than the system size. For this reason, the fluid model can be used efficiently at high pressures.

3.2 PIC/MCC Model

In the kinetic approach, the behavior of charged particles is investigated by the velocity distribution function, $f(\mathbf{r}, \mathbf{v}, t)$. In the plasma, this function is affected by external fields and collisions between particles. The distribution function is mathematically described by the Boltzmann equation (Eq. 1.1). Many methods have been developed for solving this equation up to now [61–64]. As an alternative to the direct solution of Boltzmann equation, particle simulation methods can also be used. The solution of the Boltzmann equation gives essentially the same result as the particle simulation methods. The link between them has been shown in many studies [65, 66].

Among these particle simulation methods, the PIC/MCC model can be used to express the motion of particles. The kinetic approach is necessary in order to be able to investigate the non-local or the low-pressure plasma. Since the simulation of actual number of particles in plasma is not manageable, the PIC/MCC model uses the

super particle concept [5, 6, 67] which reduces the particle number to tractable level. Generally, a super particle contains real particles ranging from 10^5 to 10^7 in one dimensional simulations. It is also a further advantage of this model that the particle densities can be interpolated into the grids (or cells) and, thus the fields can then be easily interpolated into the positions of the particles.

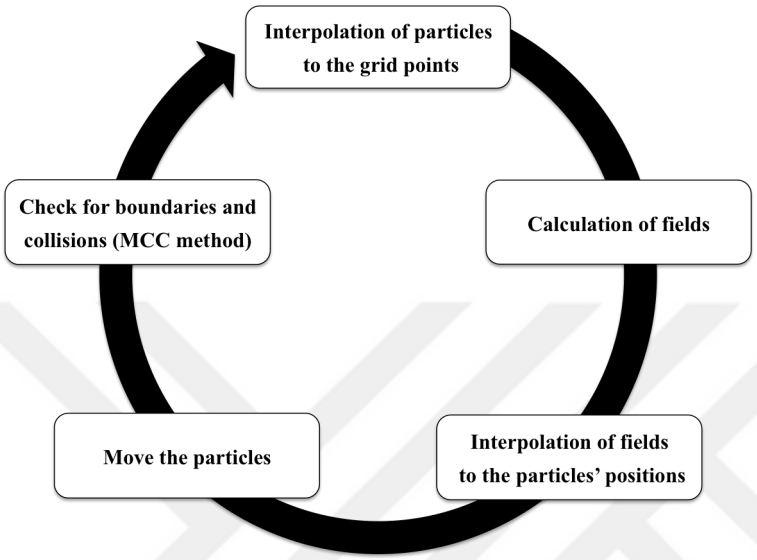


Figure 3.3: Algorithm of PIC/MCC model.

Fig. 3.3 shows the general algorithm of the PIC / MCC model. As shown, in this model, firstly, the particles that initially uniformly distributed between the electrodes are addressed by interpolating them into the grids. So that the particle densities in the grids can be calculated. These densities are used in the Poisson equation, which has the form

$$\nabla^2\phi = -\rho/\varepsilon_0, \tag{3.18}$$

to obtain the potential distribution corresponding to the density distribution of the particles. The resulting potential distribution helps to find the electric field in the grids as

$$\mathbf{E} = -\nabla\phi. \tag{3.19}$$

In the present work, magnetic field is ignored. In order to be able to update particle positions and velocities, the force acting on the particles must be known. For this reason, the electric field is interpolated to the positions of the particles. Thus, motion is governed by the Newton-Lorentz equation, which is

$$m\frac{d^2\mathbf{r}}{dt^2} = q\mathbf{E}. \tag{3.20}$$

After the calculation of the new velocities and positions of the particles is done, it is necessary to examine the collisions that particles are likely to make between themselves and at the boundaries. These collisions are checked with the Monte Carlo Collision (MCC) method. As it is known, it is a time-consuming process to examine each super particle by this method. For this reason, checking for collisions are accelerated by null collision technique [9, 11]. After this step, the loop in Fig. 3.3 is completed and all the operations in this cycle are repeated in sequence for each time step.

As can be seen, the PIC/MCC model allows for the examination of particles' behaviour with very few assumptions (super particle concept, dimensional constraints, etc.). In this model, generally, ions and electrons are simulated, while neutrals are assumed to have a uniform distribution in the background. For the model to be stable and accurate, there are some limitations on the time step and grid size [10, 68]. While the grid size must not exceed the Debye length ($\Delta x \sim \lambda_D$), the time step must not exceed the shortest time scale of the plasma (which is period of the electron plasma oscillation). More restrictively, the condition has the form

$$w_p \Delta t \leq 0.2, \tag{3.21}$$

where, $w_p = \sqrt{n_e e^2/m\varepsilon_0}$. Time step is also limited by the Courant condition,

$$v_{max}\Delta t \leq \Delta x. \tag{3.22}$$

In addition to these conditions, when a time step interval is being set, a particle must not make more than one collision per time step.

Although the PIC/MCC model is successfully described the kinetic behavior of particles in non-local plasma, it does not provide much benefit in terms of time. In order to shorten the simulation time, it is reasonable to decrease the number of super particles and increase the weighting value (real particle number per super particle), but this also has a limit. Reducing the weighting value increases the noise level, which causes the numerical heating of the particles [69, 70]. This causes misleading simulation results to be obtained. For this reason, to disable this non-physical energy, we need to have a sufficient number of super particles per Debye length ($N_D \gg 1$), which means that it is necessary to increase the number of super particles to an adequate amount, and this case prevents the use of complex chemical reactions and various plasma particles in the model. For more information about PIC/MCC model, see the paper of Verboncoeur [71].

Application of some speed up methods such as subcycling [5, 72], reduced ion mass and improved initial density profiles [10] to the code can shorten the PIC/MCC simulation time. Since ions are much heavier than electrons, moving ions less frequently does not affect the simulation results ($\Delta t_i = k\Delta t_e$). $\Delta t_i/\Delta t_e$ ratio varies with the ion mass. Δt_i and Δt_e denote the time step for ions and electrons. This method is called "subcycling". Another method of acceleration is to adjust the initial density distribution so that it is close to the value of the equilibrium density distribution. In order to be able to use this method, the density distribution in the equilibrium must be predicted analytically.

In addition, acceleration of the simulation can be achieved by reducing artifically the mass of the ion. This method can be applied in two steps. First, the calculation is continued until the equilibrium is reached with the reduced ion mass. After light-ion-equilibrium is obtained, the mass of the ions is reduced by a factor of $(m_{real}/m_{light})^{1/2}$ to return to the real ion mass value, and the calculation is resumed until the equilibrium is reached. However, the reduction of the mass of the ion causes the accelerations of them and the rate of loss of the ions to increase. This loss is compensated by increasing the electron-neutral cross-section value by $(m_{real}/m_{light})^{1/2}$. For more information about the speed-up methods, Ref. [10] can be referred.

3.3 Hybrid Model

The hybrid model is formed by coupling kinetic models and fluid models together. So that the advantages of different methods are combined. For example, while electrons are modeled with kinetic models, ions can be examined with a fluid model [73]. Or, while working with fast electrons using the kinetic methods, the efficiency can be increased by using the fluid model for ions and slow electrons [74, 75]. These situations can change according to the physics to be studied. The point to note here is that the time steps required for the kinetic and fluid models are different [76]. Therefore, by using different approaches, it is necessary to make the communication between these two models efficiently.

The hybrid model is not as fast as the fluid model, although it is more advantageous to explain the kinetic behavior of the particles. Also, this model is not as time consuming as the PIC model. For more information, see Ref. [77].

As indicated, each model can be advantageous or disadvantageous according to different physical conditions. For more information about these three models and their applications, see the work of Kim et al. [76].

CHAPTER 4

PIC/MCC CODE

In the present study, the PIC/MCC code was prepared to perform detailed studies on non-local plasma. The code is written in Fortran 90 language. In the code, a Cartesian coordinate system is used, and the position has been added to the calculations as 1 dimensional and velocity as 3 dimensional (so called 1d3v code). Before beginning the PIC/MCC cycle (Fig. 3.3), the particles must initially have a certain velocity and position distribution. It is assumed that the particles initially have a uniform position distribution. In order to achieve this uniformity, a random number generator which distributed the random numbers uniformly between 0 and 1 was used. Fig. 4.1 shows an example of a uniform position distribution obtained by random number generator.

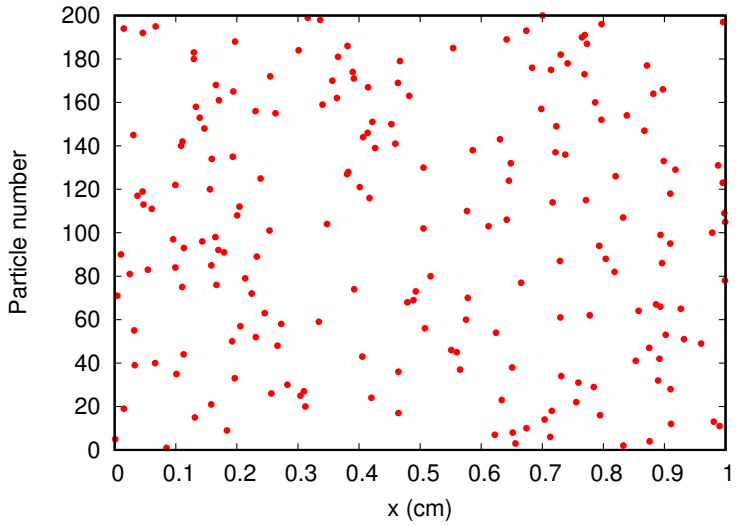


Figure 4.1: Uniform distribution of the position of 200 particles obtained by random number generator.

In addition, the velocities of the particles are assumed to have initially a Maxwellian

distribution. With this distribution, velocity components have the form as

$$v_i = \sqrt{-ln(R_1)2k_BT/m}\sin(2\pi R_2), \tag{4.1}$$

where, v_i is the velocity component (v_x, v_y, v_z). R_1 and R_2 represent random numbers that are uniformly distributed between 0 and 1. After the initial velocity and position values of the particles are determined, the charge assignment process which is the first step of the PIC/MCC model, is performed. The methods and assumptions used in the steps of the model are explained in detail in the following sections.

4.1 Charge Assignment

Interpolating the positions of the particles into the grids allows the distribution of the particles to be examined and the electric field to be easily calculated.

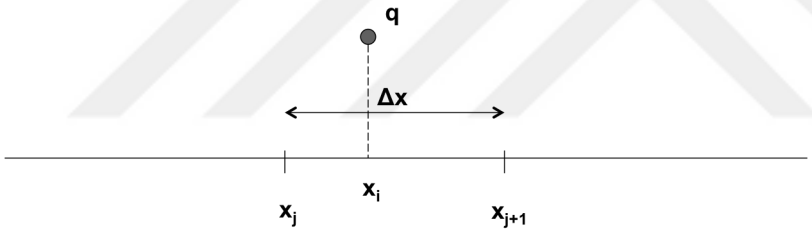


Figure 4.2: Assigning charges to the grid points.

In Fig. 4.2, a particle is located between two grid points and closer to the jth grid. According to the first order weighting method, $x_{j+1} - x_i$ part contributes to the jth grid while $x_i - x_j$ part contributes to the $(j+1)$th grid. By taking this method into consideration, the weighting equations for the charge density are obtained as

$$\rho_j = \rho_j + qw\frac{x_{j+1} - x_i}{(\Delta x)^2}, \tag{4.2}$$

$$\rho_{j+1} = \rho_{j+1} + qw\frac{x_i - x_j}{(\Delta x)^2}. \tag{4.3}$$

4.2 Motion of Particles

In order to move the particles, first, the Poisson equation (Eqn. 3.18) must be solved numerically and the potential distribution corresponding to the charge density in the grids must be obtained. This numerical solution is obtained using the tridiagonal matrix algorithm (TDMA), also known as the Thomas algorithm [78]. For this purpose, a one-dimensional Poisson equation is transformed into a matrix equation which has the form

$$\begin{bmatrix} 2 & -1 & 0 & \dots & 0 \\ -1 & 2 & -1 & \dots & 0 \\ \vdots & \vdots & \vdots & \ddots & \vdots \\ 0 & \dots & -1 & 2 & -1 \\ 0 & \dots & 0 & -1 & 2 \end{bmatrix} \begin{bmatrix} \phi_2 \\ \phi_3 \\ \vdots \\ \phi_{N-2} \\ \phi_{N-1} \end{bmatrix} = \begin{bmatrix} (\rho_2/\varepsilon_0)(\Delta x)^2 + \phi_{left} \\ (\rho_3/\varepsilon_0)(\Delta x)^2 \\ \vdots \\ (\rho_{N-2}/\varepsilon_0)(\Delta x)^2 \\ (\rho_{N-1}/\varepsilon_0)(\Delta x)^2 + \phi_{right} \end{bmatrix}, \tag{4.4}$$

by transforming it into a discrete form by using the central difference approximation,

$$\frac{\phi_{j-1} - 2\phi_j + \phi_{j+1}}{(\Delta x)^2} = -\frac{\rho_j}{\varepsilon_0}. \tag{4.5}$$

Then, by using TDMA, after forward elimination in the matrix, the solution is obtained by backward subtitution. After this calculation, another step is the calculation of the electric field, which causes the particles to move. For this calculation, Eqn. 3.19 is rearranged in the form

$$E_j = -\left(\frac{\phi_{j+1} - \phi_{j-1}}{2\Delta x}\right), \tag{4.6}$$

by using the central difference approximation again and the electric field values in the grid points are calculated. In order to move each particle, these values must be interpolated to the positions of the particles. This is done by using the first order weighting method, as described in Section 4.1. Thus, the electric field affecting the

particles is calculated as

$$E_i = \frac{(x_i - x_j)}{\Delta x} E_{j+1} + \frac{(x_{j+1} - x_i)}{\Delta x} E_j. \tag{4.7}$$

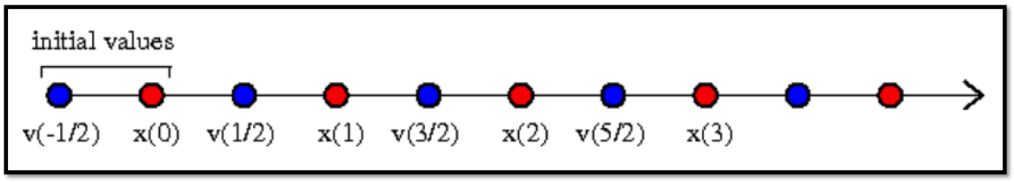


Figure 4.3: The scheme of the leapfrog method.

The new positions and velocities can be calculated by the Lorentz equation (Eqn. 3.20). The Leapfrog algorithm, a second-order method, is used to solve this equation. The scheme of this algorithm is shown in Fig. 4.3. Accordingly, after the initial values for velocity ($v_{1/2}$) and position (x_0) are calculated, the values for the next time step are obtained by leapfrogging over each other. The corresponding equations of motion have the form,

$$x_{n+1} = x_n + v_{n+1/2}\Delta t, \tag{4.8}$$

$$v_{n+1/2} = v_{n-1/2} + \frac{F(x_n)\Delta t}{m}. \tag{4.9}$$

With these equations of motion, the particles are moved and the updated velocity and position values of the particles are obtained.

The fragment of the code, particle mover part described in this section, has been tested by simulating the well-known two stream instability. This phenomenon can be caused by two currents moving in opposite directions and at a certain velocity. The parameters and initial conditions used in this simulation are taken from the work of Fitzpatrick [79] in order to compare the results. The initial velocity distribution of the particles is arranged in accordance with the probability distribution function [79]

which has the form

$$f(x,v) = \frac{n_0}{2}\left\{\frac{1}{\sqrt{2\pi}v_{th}}e^{-(v-v_b)^2/2v_{th}^2} + \frac{1}{\sqrt{2\pi}v_{th}}e^{-(v+v_b)^2/2v_{th}^2}\right\}, \tag{4.10}$$

where v_{th} is the thermal velocity and is taken as 1 because the physical quantities in this simulation are normalized. Also, n_0 and v_b are the initial number density and the mean velocity, respectively. The mean velocity must be much greater than the thermal velocity in order for the instability to occur. The parameters [79] used in this simulation and their values are summarized in Table 4.1.

Table 4.1: The parameters used in the PIC/MCC simulation of two stream instability [79].

Number of particles	20000
Mean velocity (v_b)	3
Grid Number	1000
Distance	100
Time step	0.1

The comparison of the electron phase space distributions obtained from this study with the published simulation results [79] is shown in Fig. 4.4 and Fig. 4.5. As can be seen, the two streams that initially have a uniform distribution are deteriorating over time. As time passes, instability becomes even more pronounced. Also, as a result of comparison, the resulting graphs seem to be consistent with published ones, except for negligible differences. The use of different programming language and different seed values of random number generators can cause such differences.

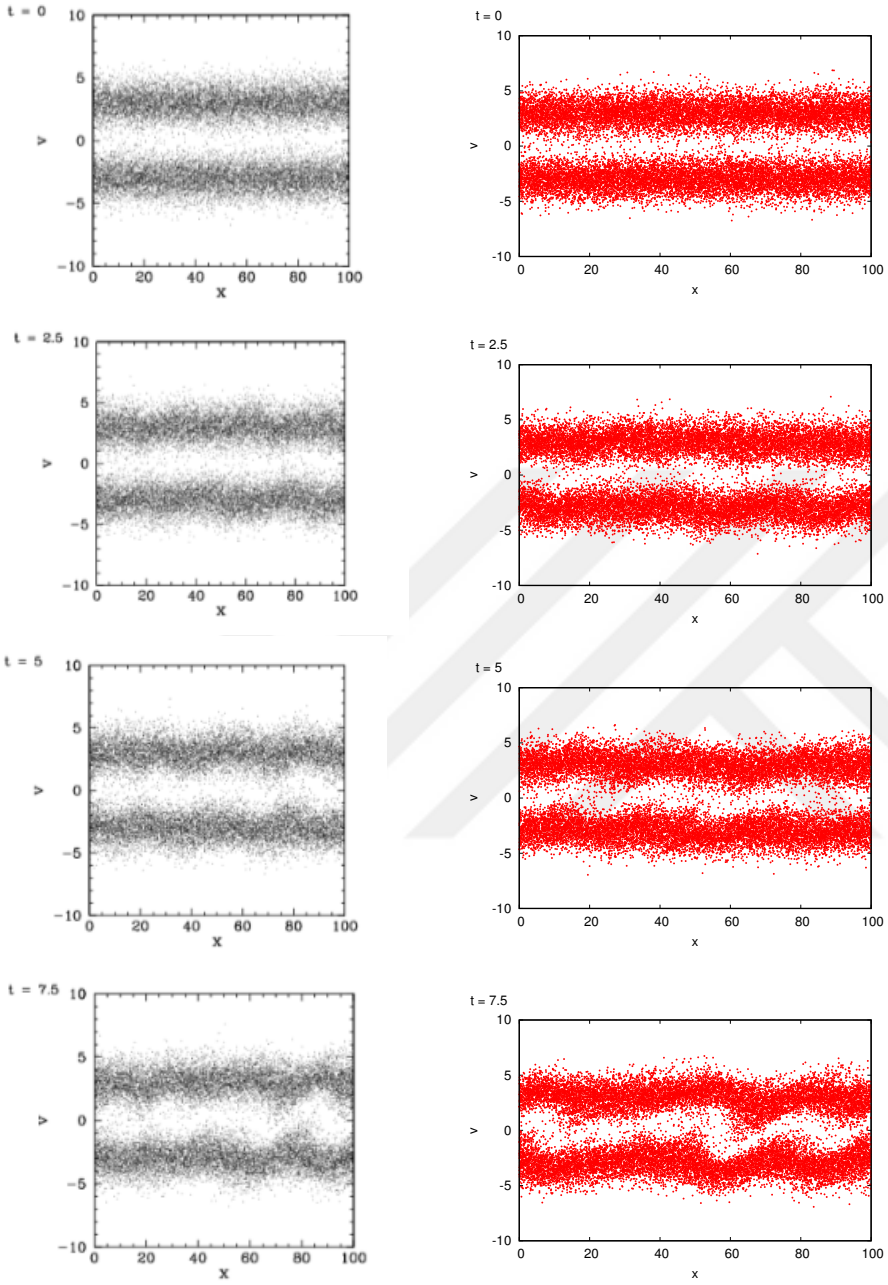


Figure 4.4: The electron phase space distribution obtained at $t = 0, 2.5, 5$ and 7.5. The graphs on the left are taken from the work of Fitzpatrick [79] and the ones on the right are the results of the current study.

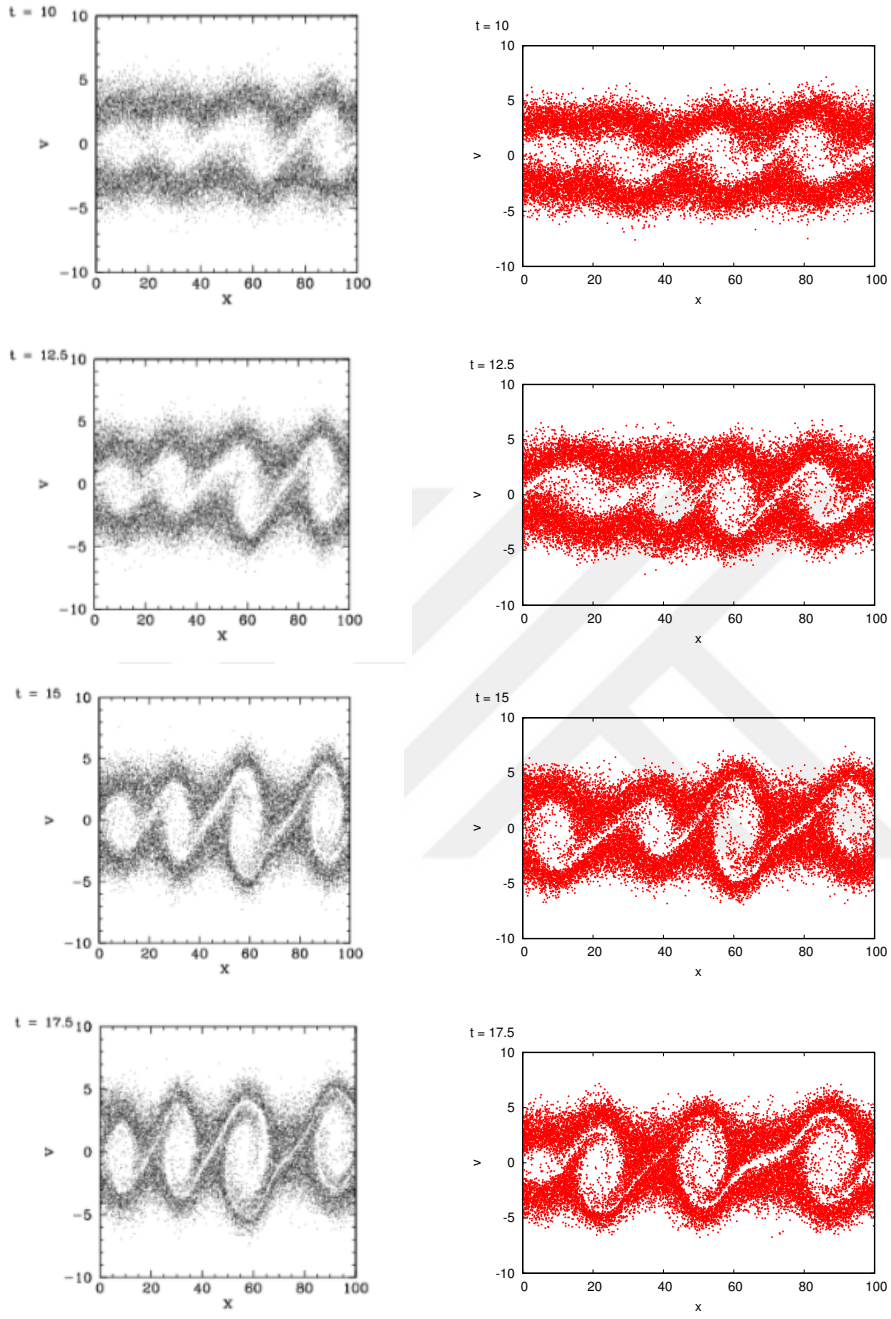


Figure 4.5: The electron phase space distribution obtained at $t = 10, 12.5, 15$ and 17.5. The graphs on the left are taken from the work of Fitzpatrick [79] and the ones on the right are the results of the current study.

4.3 Collisions and Boundary Conditions

Collisions and boundary conditions are examined through the MCC method. Particles can make collisions between each other, as well as reactions at the boundaries. A cross-section value (σ) defines the probability of each collision type. With this value, the probability of any collision is defined as

$$P = 1 - \exp(-n\sigma v\Delta t). \tag{4.11}$$

In this equation, n and v are the neutral density and the velocity of particle, respectively. In collisions between electrons and neutrals, neutrals are assumed to be at rest. For this reason, only the speed of electrons is taken into account in the probability equation. However, in the case of collisions between ions and neutrals, this approximation loses its validity. In such a case, the probability is calculated by finding the velocity of ions relative to neutrals.

According to the MCC method, random numbers with a uniform distribution between 0 and 1 are compared with the probability of collision, in order to understand whether the collision is to occur. Providing the condition,

$$R \leq P, \tag{4.12}$$

means that a collision was occured. However, as mentioned in the Introduction, because it takes a lot of time to repeat this process for each super particle, the null collision technique [9, 11], which speeds up this process, is very beneficial in this part. In order to use this technique, first, the collision frequencies, ν, are calculated for all particles separately as

$$\nu = n\sigma_t v, \tag{4.13}$$

where σ_t is the total cross section, and then the maximum frequency value can be determined. When this value is substituted in Eqn. 4.11, the maximum probability is obtained and thus the maximum number of collisions, NP_{max}, is determined. With

this maximum number of collisions, only the maximum number of randomly chosen particles are checked for possible collisions. However, there are some differences in this checking process. Since not all of the super particles are used in this process, the probability of any collision must now have the form,

$$P = \frac{1 - \exp(-n\sigma v \Delta t)}{1 - \exp(-N P_{max} \Delta t)}. \tag{4.14}$$

For a sufficiently small time step, this equation can be rewritten as

$$P = \frac{n\sigma v}{N P_{max}}. \tag{4.15}$$

Thus, the probability for each type of collision is calculated separately and the types of collisions are determined by using random numbers. In the existing code, this technique is used and the efficiency is increased. Besides, when the particles strike the electrodes, they can be absorbed, reflected back, or cause a secondary electron to be released. Each electrode is characterized by coefficients that define the probabilities of these reactions. The reflection of particles is defined by the reflection coefficient (r) and the release of a secondary electron by the secondary electron emission coefficient (γ). In the absence of these two phenomena, it is assumed that the particles are absorbed at the boundaries. Since these are small coefficients, they can be compared directly with random numbers to determine what kind of reactions the particles cause.

The particles are scattered after the collision. This scattering is assumed to be isotropic and is expressed by two angles: the scattering angle χ , and azimuth angle η , which usually have the form

$$\chi = \arccos(1 - 2R), \tag{4.16}$$

$$\eta = 2\pi R. \tag{4.17}$$

Here, R is the random number distributed uniformly between 0 and 1. Using these

angles, the velocity vector after the collision is obtained as [80]

$$\mathbf{v}_{after} = \mathbf{v}_{before} \begin{bmatrix} \cos\chi \\ \sin\chi\cos\eta \\ \sin\chi\sin\eta \end{bmatrix}. \tag{4.18}$$

In order to test the collision part of the code, a Townsend discharge simulation was performed. Townsend discharge is the phenomenon where electrons multiply as a result of collisions with neutrals when moving in a homogeneous electric field. In this simulation, the motion of electrons in Ar gas under 1 Torr pressure is investigated. Even though the homogeneous electric field is in the x direction, the motion of the particles is analyzed in 3d3v. The reduced electric field (E/n) is taken as 500 Td, where $1\,Td = 10^{-21}\,Vm^2$, and the distance between the electrodes (L) is taken as 1 cm. Initially, 500000 electrons were assumed to be emitted by the cathode with 1 eV energy. The simulation was continued until all electrons were absorbed by the anode. It is assumed that only elastic, excitation and ionization processes occur between electrons and neutrals. The cross-section graphs [81] corresponding to these collision types are shown in Fig. 4.6.

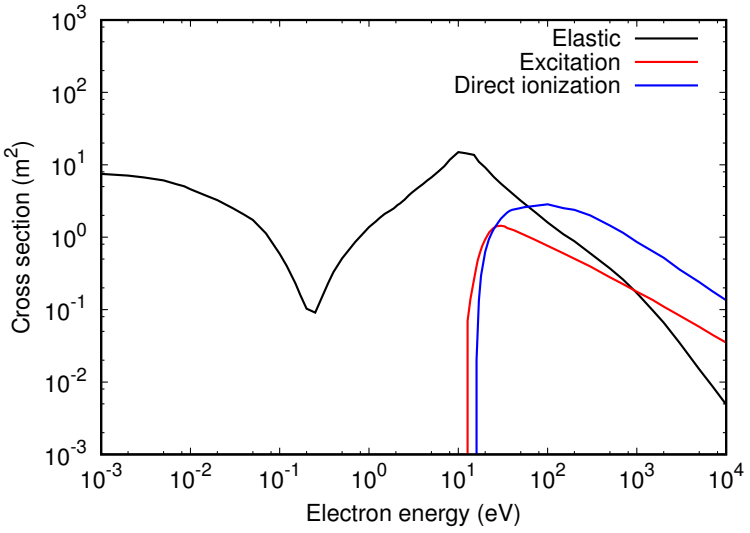
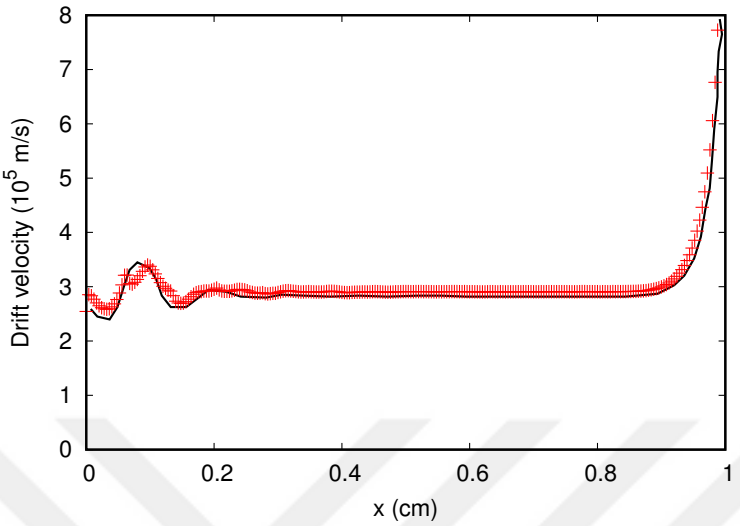


Figure 4.6: Electron cross-sections [81] in argon gas used in the townsend discharge simulation.

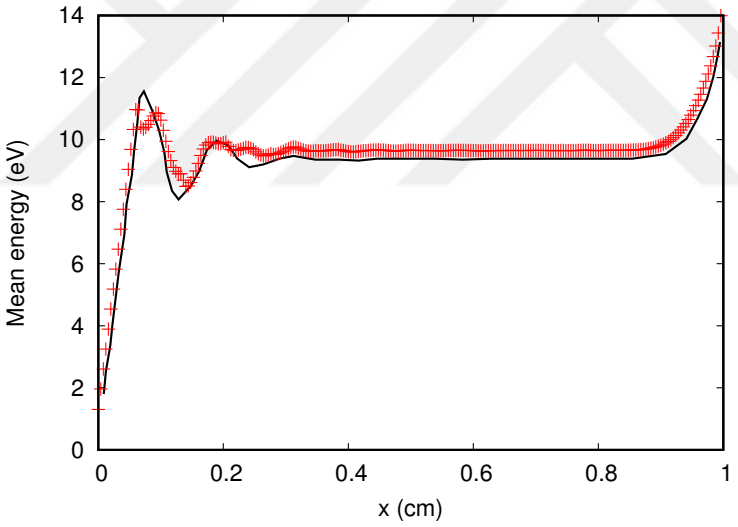
All simulation parameters are taken from the study of Donko [80] in order to compare the results. As a result of this study, the graphs for mean energy, $\langle\varepsilon\rangle$, drift velocity, v_{dr}, and Townsend's ionization coefficient, α, which describe the motion of the electrons, have been obtained. The Townsend's coefficient is determined from the drift energy gained by the electric field and has the form

$$\alpha = \frac{d\Gamma(x)}{\Gamma(x)dx}. \tag{4.19}$$

The graphs obtained from this simulation, compared with previous results [80], are shown in Fig. 4.7 and Fig. 4.8. The first thing that stands out in the graphs is that the homogeneous electric field does not cause a homogeneous motion. As can be seen, there are three separate zones. Near the cathode, there are fluctuations because the electrons are accelerating. While the particles reach the equilibrium in the middle, homogeneity deteriorates around the anode as the particles start to be absorbed by the anode. Also, as a result of comparison, the results obtained from this simulation appear to be in agreement with the results obtained from Donko's study [80].



(a)



(b)

Figure 4.7: The drift velocity (a) and the mean energy (b) profiles obtained as a result of the Townsend discharge simulation. Solid line corresponds to the result from Ref. [80].

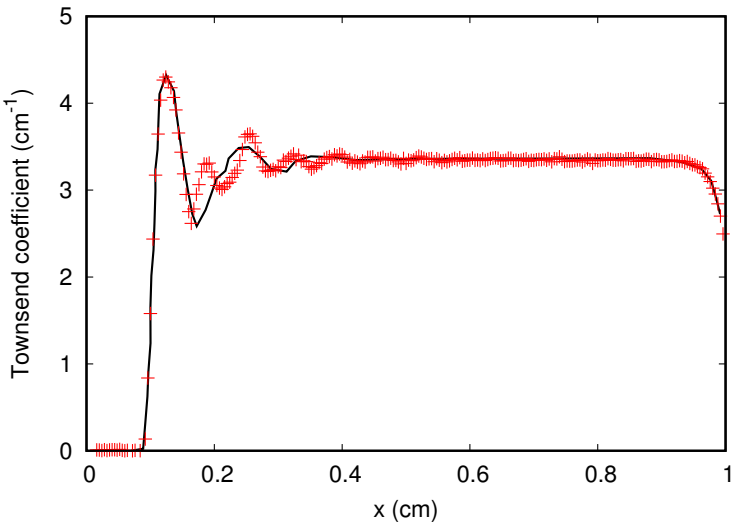


Figure 4.8: Townsend coefficient profile obtained as a result of the Townsend discharge simulation. Solid line corresponds to the result from Ref. [80].

4.4 Validation of the PIC/MCC Code

The fact that each part of the code has been verified does not mean that the code works correctly as a whole. Communication between these parts should also be tested. To this end, the currently developed 1d3v PIC/MCC code is adapted to capacitively coupled Radio-Frequency (RF) glow discharge in helium gas by using the parameters of the study of Turner et al. [82]. As it is known, electrodes used in dc glow discharge have to be conducting in order for the plasma to be sustainable. However, when the electrodes are not conducting, for example when a spectrochemical analysis of a non-conducting material is desired, the charged particles accumulate on the electrodes as they impact them. In this case, the plasma can not be sustainable. The only solution to this is to apply a varying voltage between the electrodes. Thus, each electrode, in turn, can be an anode and a cathode. Charges that accumulate when the electrode is cathode become neutralized by combining with opposing charges that will accumulate when the same electrode is then anode. Therefore, in RF discharge, while one of the electrodes is grounded, the voltage applied to the other electrode varies

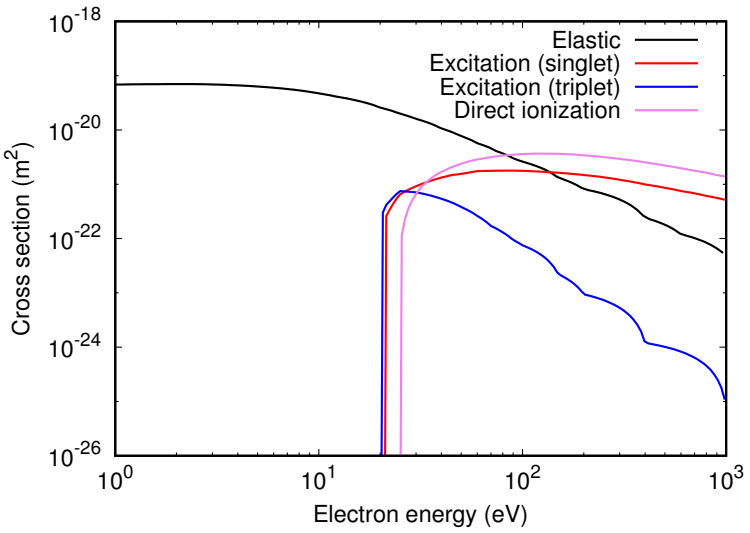


Figure 4.9: Electron cross-sections in helium gas used in the validation of PIC/MCC code [83].

sinusoidally as

$$\phi = \phi_0 \sin(2\pi f t), \tag{4.20}$$

where f is the frequency. In this test, reactions such as secondary electron emission and reflection in boundaries are neglected. Among the collisions between the electrons and the neutrals, elastic, singlet excitation, triplet excitation and ionization are taken into consideration, and the graph containing the cross-section data [83] corresponding to these collisions is seen in Fig. 4.9.

In addition, the isotropic and backward scattering are considered between ions and neutrals, and the cross-section data corresponding to these collision types are obtained by [84]

$$\sigma_{iso} = 7.63 \times 10^{-20} \left(\varepsilon_{rel}^{-0.5}\right), \tag{4.21}$$

and

$$\sigma_{back} = 10^{-19} \left(10^{-3}\varepsilon_{rel}\right)^{-0.15} \left(1 + 10^{-3}\varepsilon_{rel}\right)^{-0.25} \left(1 + 5\varepsilon_{rel}^{-1}\right)^{-0.15}. \tag{4.22}$$

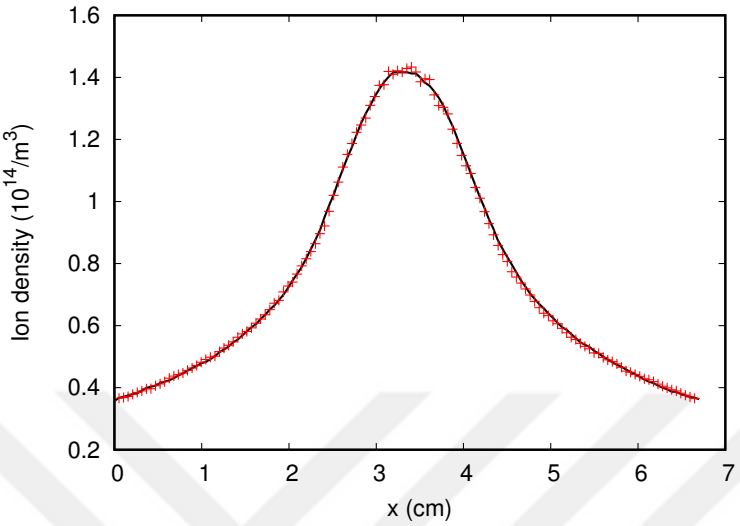
Here, the unit of cross-sections is m^2 and ε_{rel} is the relative energy of ion to that of

Table 4.2: The parameters [82] used for validation of the 1d3v PIC/MCC code.

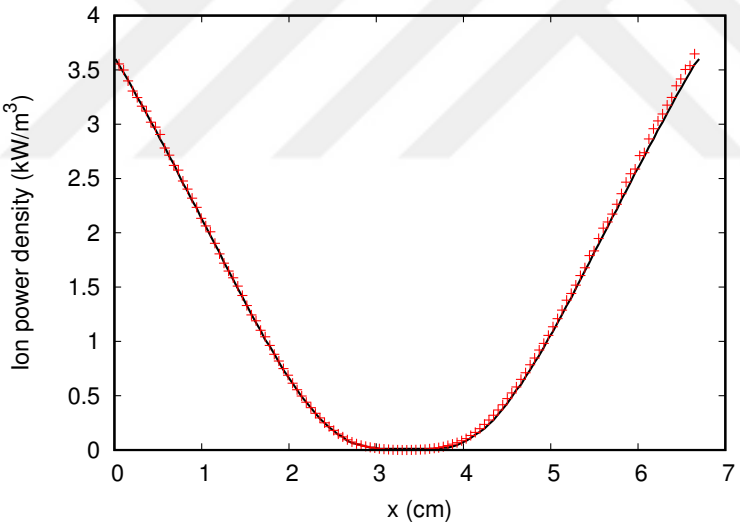
Initial plasma density ($10^{14} m^{-3}$)	2.56
Initial electron temperature (K)	30000
Initial ion temperature (K)	300
Initial number of particles per cell	512
Neutral temperature (K)	300
Neutral density ($10^{20} m^{-3}$)	9.64
Voltage amplitude (V)	450
Inter-electrode distance, L (cm)	6.7
Frequency, f (MHz)	13.56
Simulation time (s)	$1280/f$
Averaging time (s)	$32/f$
Cell size, Δx (m)	$L/128$
Time step size, Δt (s)	$(400f)^{-1}$

neutral (in eV). The parameters [82] used for validation are summarized in Table 4.2.

The results of this simulation are shown in Fig. 4.10, compared with published results. According to the Turner et al. [82], the ions are very sensitive to the numerical techniques used. For this reason, ion density and ion power density profiles were compared. In addition, the profile of ion density is also compared with the profiles obtained from the codes written by different authors [82] in Fig. 4.11. The results [85] of the comparison supports the validity of the code.



(a)



(b)

Figure 4.10: Ion (a) and ion power densities (b) obtained as a result of the validation test. Solid line corresponds to the result from Ref. [82].

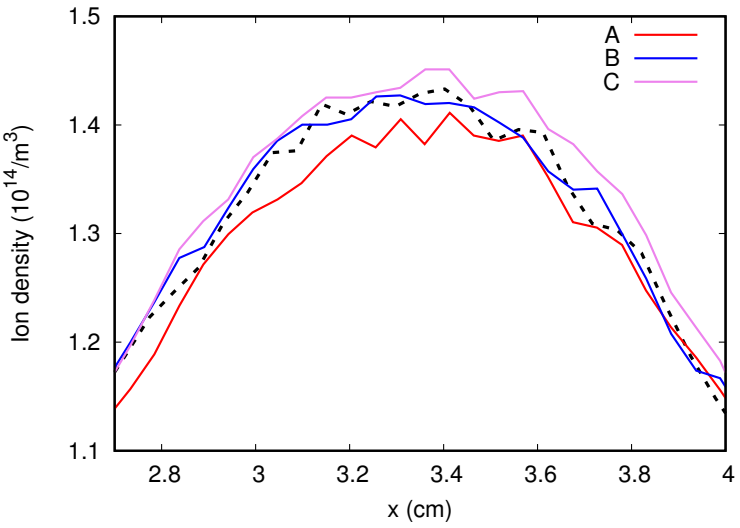


Figure 4.11: Comparison of the ion density distribution profile with the results obtained in Ref. [82]. Dashed line corresponds to the result obtained from the current work. The curves labelled A to C obtained by Turner, Derzsi and Donko, Mussenbrock, respectively.

4.5 Parallelization of the PIC/MCC Code

Nowadays, along with the development of computer processors, parallel calculations have taken the place of serial calculations. As it is known, in serial computations, only one task can be performed at a certain time and tasks can only be completed one after another. Such a calculation requires a lot of time. With progressive technology, Central Processing Units (CPUs) with multiple cores are offered for use and these CPUs allow multiple tasks to be completed at a given time.

Communication libraries are needed to realize the parallel computing. These libraries are divided into two according to the memory usage. Libraries that use shared memory are OpenMP and Pthreads, while those using distributed memory are OpenMPI and PVM. In the current work, 1d3v PIC/MCC code is parallelized using OpenMPI. The advantage of OpenMPI is that each processor uses its own memory. Thus, the processors can work independently from each other, which means that they do not have to constantly communicate with each other. When to do synchronization between tasks is totally optional. This is an effect that increases the efficiency of paral-

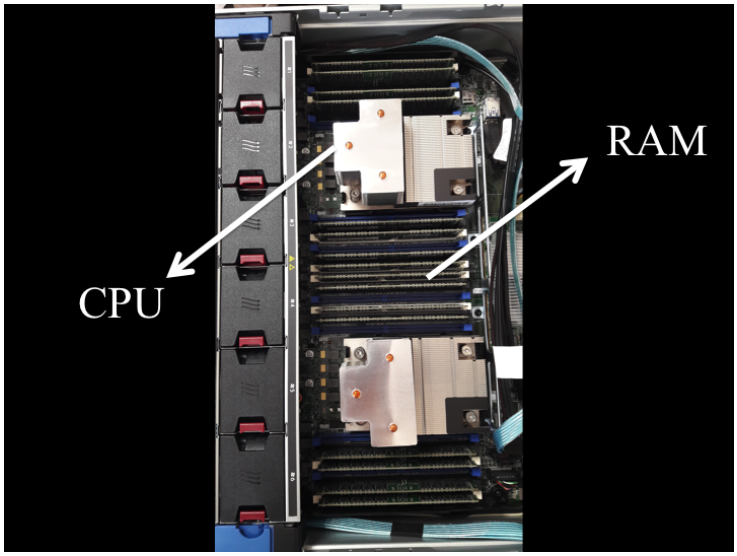


Figure 4.12: Inside view of a server in the present technology.

lelization. However, it is not always possible to parallelize the entire code. In such a case, let p be the parallellable fraction of the code. Thus, the part that can not be done in parallel is $1-p$. If we are going to run this code on a computer with n processors, the time required to complete the program will be $(1-p+p/n)$ of the time required for serial computation.

In this work, parallelization was performed by initially distributing the particles to the processors. In this parallel code, each processor moves its own particles and checks for possible collisions. Only in the Poisson solution step, interprocessor communication is provided to obtain the total particle density. By using this value, the potential and electric field distributions are calculated and broadcasted to all processors. Then, again, each processor continues its calculations for its own particles.

Table 4.3: The parameters [82] used in the parallelization test.

Weighting	3.0×10^7
Voltage (V)	500
Frequency (MHz)	1.5
Cell number	600
Pressure (Pa)	46
SEE coefficient, γ	0.3
Reflection coefficient, r	0.25

The data used in the parallelization process is summarized in Table 4.3. As can be seen, the secondary electron emission (SEE) from the cathode, and the reflection of electrons from the anode are taken into account in this study. The time required for the code to complete calculations is examined by changing the number of cores. The speed up obtained by increasing the number of cores is calculated as

$$Speed\,up(N_p) = \frac{T(1)}{T(N_p)}, \tag{4.23}$$

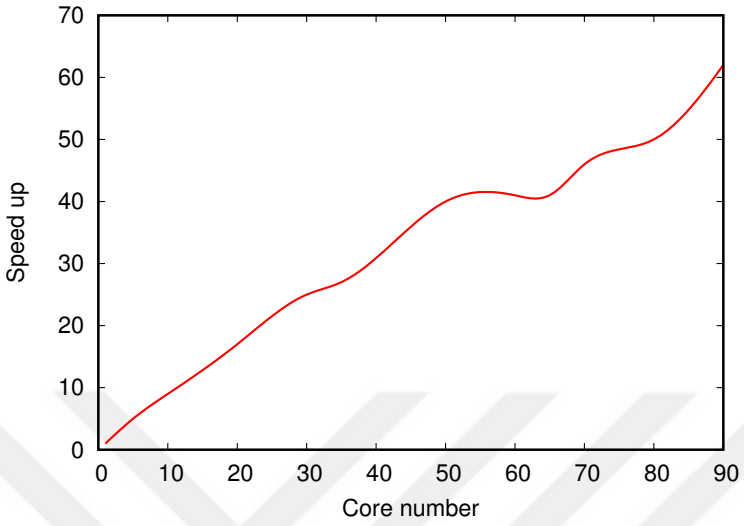
and the efficiency corresponding to this speed up is calculated as

$$Efficiency = \frac{Speed\,up(N_p)}{N_p}. \tag{4.24}$$

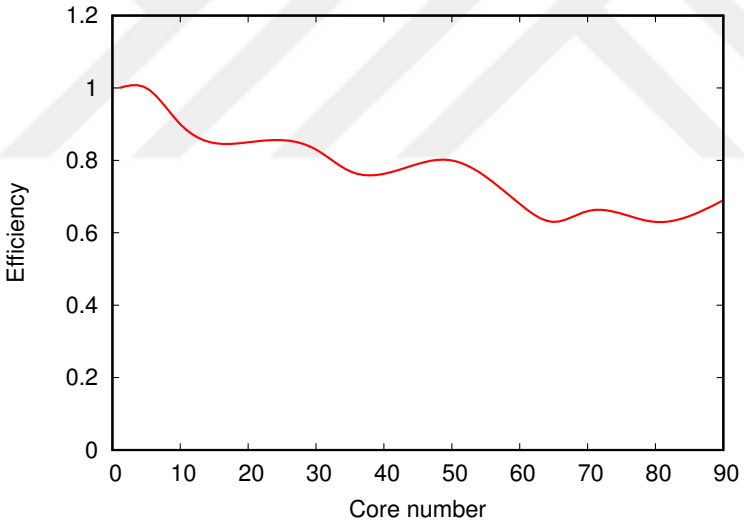
In these equations, N_p, $T(1)$ and $T(N_p)$ are the number of processors, the time required to complete the job on one processor and the time required to complete the job on N_p processors, respectively.

The graphs of speed up and efficiency obtained in this study are shown in Fig. 4.13. As can be seen from these figures, the performance is increased about 60 times when 90 cores are used [86]. However, the yield obtained when fewer cores are used decreases as the number of cores increases.

The increase in the number of cores means that more time is spent for synchronization between the cores. Synchronization is of great importance if there are some parts of the code that are not parallelized. In the existing code, the presence of such parts (poisson solution and electric field calculation) explains the drop in performance. In addition, an increase in the number of cores leads to inequality in the number of particles per core. This also causes performance loss in the code.



(a)



(b)

Figure 4.13: Speed up (a) and efficiency (b) graphs obtained as a result of the parallelization of the code.

4.6 Conclusion

The 1d3v PIC/MCC code was developed with the Fortran 90 language environment. The motion and collisions of particles are tested and validated with well known two stream instability and townsend discharge events. Then, by simulating RF capacitive glow discharge in helium gas, the results were compared to the published results. As a result of this comparison, the applicability of the code was verified. The excessive time consumption which is the disadvantage of the PIC/MCC model, is shortened by making the code parallel by using OpenMPI library. As a result of the parallelization process, when 90 cores were used, the performance of the code was increased 60 times.

CHAPTER 5

SIMULATION OF THE PHOTORESONANCE PLASMA

The photoresonance plasma is basically the phenomenon of the formation of the plasma as a result of the resonant absorption of the light. As in the PLES method, charged particles are formed mainly by Penning ionization. As mentioned in the Introduction, the availability of such a plasma as a photoelectric converter is a promising research topic.

Systematic studies on photoplasma began in 1967 by Morgulis, Korchevoi and Przhonskii [25], although it was first discovered in 1930 [24]. As a result of subsequent studies [26–28], information about the mechanisms of processes involving excited atoms could be obtained. The most important advantage of the photoplasma is the possibility of being used as a photoelectric converter. For example, Brandenberger [29] observed a photo emf in the microwave discharge in Krypton. For a 1 mW laser power, they were able to achieve a potential difference of approximately 0.1 V. In recent studies [30, 31] using ambipolar potential difference method, about 3-4 V photo-emf could be obtained with laser light. This potential difference is almost one order of magnitude higher than that for semiconductor converters. These results have been promising that the photoplasma can also be used to convert solar radiation into electricity.

Dunning and Palmer [34] performed the first experiment for this plasma converters based on the MHD generators by heating cesium vapor with concentrated solar radiation using a heat pipe. However, the theoretical investigations [34, 35] on this subject is rather limited and a numerical analysis has not been done yet using a kinetic approach. Therefore, in order to understand the underlying physics of this subject in detail, parallel 1d3v PIC/MCC simulation of photoplasma in sodium alkali metal va-

por exposed to light radiation was performed. Since the alkali metal vapor, in which the photoresonance plasma is formed, has a low melting point, such gases can be used as the high temperature photoelectric collector of sunlight.

5.1 Model

In the present work, the photoresonance plasma sustained in a sodium vapor was simulated using the developed parallel 1d3v PIC/MCC code. The main mechanism of photoplasma is the resonantly excitation of neutral atoms by light. The sodium gas which is used in this model has an absorption line at 589 nm, in the visible light wavelength range. This line corresponds to 3s $\rightarrow$ 3p transition. In order to be able to use the photoresonance plasma as a photoelectric converter, the homogeneity of the plasma must be disturbed and a difference should be observed in the net amount of charges that strike the walls. In order to achieve this, the Na(3p) concentration was taken stepwise and assumed to be constant throughout the simulation. One of the reactions that take place between the metastable atoms and plays an important role in the formation of the plasma [87, 88] is the associative ionization with cross-section $4 \times 10^{-17}\, cm^2$,

$$Na(3p) + Na(3p) \rightarrow Na_2^+ + e. \tag{5.1}$$

Another reaction is the Penning ionization with cross-section $1 \times 10^{-12}\, cm^2$,

$$Na(nl) + Na(3p) \rightarrow Na^+ + Na(3s) + e, \tag{5.2}$$

which takes place between Na(3p) and the excited atom that occurs in the excitation reaction with cross-section $1 \times 10^{-15}\, cm^2$,

$$Na(3p) + Na(3p) \rightarrow Na(nl) + Na(3s). \tag{5.3}$$

According to the study of Carre et al. [88], Na(5s) and Na(4p) atoms take part dominantly in Penning ionization. For simplicity, Na(5s) was taken into account only in

the simulation. Among the electrons and neutrals, the reactions considered in the model are the elastic [89], excitation and stepwise (from the resonance level) ionization [90] collisions (see Fig. 5.1). In addition, the isotropic and backward scattering processes [91] between ions and neutrals with cross-sections $4 \times 10^{-14}\, cm^2$ and $2 \times 10^{-14}\, cm^2$, are also taken into account. Finally, the superelastic collision with the cross-section [92] $20 \times 10^{-16}\, cm^2$,

$$Na(3p) + e \rightarrow Na(3s) + e, \tag{5.4}$$

which is a reaction in which the metastable atoms can transfer their energy to electrons, is also included in the model.

The parameters used in the model are shown in Table 5.1. In this study, it is required to analyze an excess of electrons and ions on the electrodes for the determination of the potential difference between the walls. For this reason, in the solution of the Poisson equation, one of the boundaries is considered to be potentially grounded, and the potential at the other boundary is calculated by considering the surface charge density as

$$\varepsilon_0 \nabla\phi \cdot \hat{n} = -\sigma. \tag{5.5}$$

Here, σ is the surface charge density and $\hat{n}$ is the normal unit vector outward to the wall surface.

Table 5.1: The parameters used in the PIC/MCC simulation of photoresonance plasma.

Species	e, Na^+, Na_2^+
Weighting (10^7)	5
Grid number	600
Distance (cm)	1
Neutral temperature (K)	520
Neutral density ($1/m^3$)	1.4

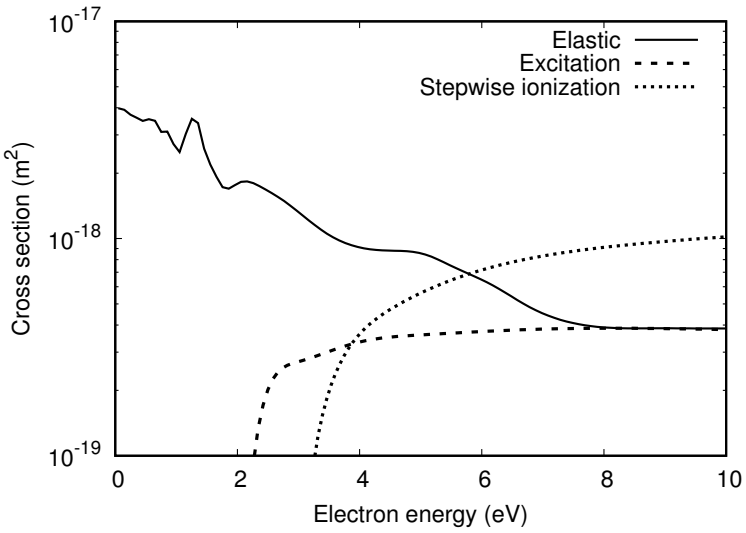


Figure 5.1: Electron cross-sections for elastic [89], excitation and stepwise ionization (from the resonance level Na(3p)) [90] collisions in sodium.

5.2 Effect of Particle Weighting

First, in order to obtain physically accurate results, studies have been conducted to determine the correct weighting value. As a result of these studies, the observed effect of the weighting on the plasma parameters is summarized in Table 5.2. As can be seen, the results obtained for four different weightings were examined when the plasma was reached a steady state. When the variation of the number of super particles is examined over time (see Fig. 5.2), it has been found that the plasma becomes stable at the 4×10^6th time step corresponding to "physical" time interval of 4×10^{-4} s. λ_D and N_D were calculated at point where the electron density is maximum. As seen in Table 5.2, when the parameters (obtained by decreasing the weighting value from 32×10^8 to 0.5×10^8) are taken into account, it is observed that the total number of particles and consequently the other parameters of the table increased by about one order in magnitude, except the Debye length.

In Fig. 5.3 and Fig. 5.4, the effect of weighting on Na^+ density, the electric potential, the EEDF and ion and electron mean energy are shown. The results show that when the weighting value is increased from 0.5×10^8 to 32×10^8, a change about 40% is observed in magnitude of the computed plasma properties. However, the results

Table 5.2: Effect of particle weighting on the total number of super electrons, the average number of super electrons per grid cell, the Debye length, λ_D, and number of super electrons per Debye length, N_D, at the steady state. λ_D and N_D were calculated about the local maximum of the electron density, using the effective temperature T_h corresponding to high energetic electron groups.

Weighting	Total number of super electrons	Averaged number of super electrons per grid cell	Debye length λ_D (m)	N_D
32×10^8	30373	51	3.69×10^{-5}	112
8×10^8	131301	219	3.51×10^{-5}	461
2×10^8	641984	1070	2.70×10^{-5}	1680
0.5×10^8	2766996	4612	2.48×10^{-5}	6490

obtained with values 2×10^8 and 0.5×10^8 vary by about 10 percent. This means that taking the weighting value of 2×10^8 is enough to get converged results. Also the number of particles per Debye length in this weighting value, $N_D = 1680$ which is statistically sufficient, supports this argument.

Furthermore, as seen in Fig. 5.4, the change in the weighting value does not cause any change in the mean energy of the ions, although it affects the EEDF and the electron mean energy.

5.3 Effect of the Courant Number

As mentioned earlier, in order for the PIC/MCC method to yield accurate results, the grid size and time step must meet the limits which have the form

$$w_p \Delta t \leq 0.2, \; v_{max}(\Delta t / \Delta x) \leq C. \tag{5.6}$$

The first condition indicates that the time step interval must resolve the frequency of electron oscillations in plasma, w_p. The second one is known as the Courant-Friedrichs-Levy condition [93] (in one dimension), which sets a limit to grid size. With this condition, it can be seen that the grid size can not be adjusted independently

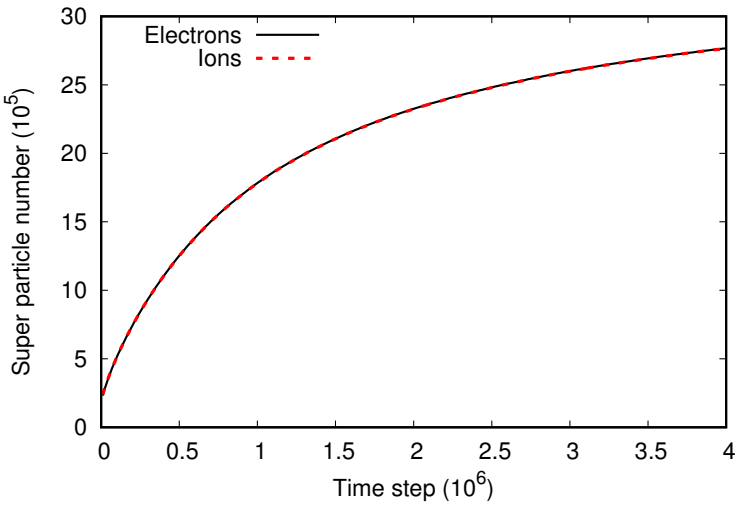
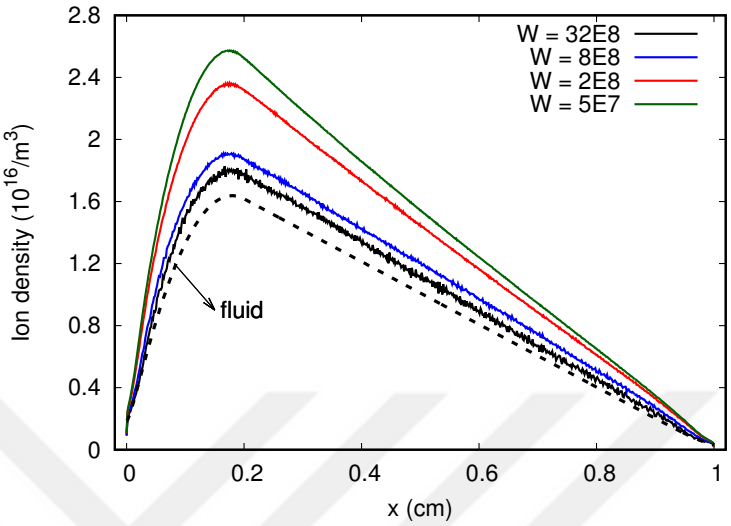


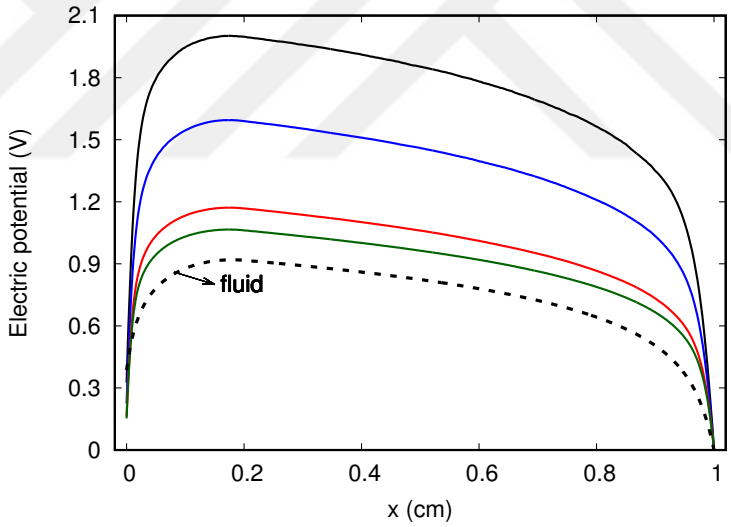
Figure 5.2: Convergence test: number of super electrons and ions versus the time step.

of the time step. Here, the constant C is known as the Courant number and varies according to the numerical method used to describe equations of motion. For example, it is known that for the explicit Eularian Leapfrog method, which is used in the present work, the Courant number is limited by 1 [94].

In order to determine the effect of Courant number in the present simulation, the simulation results are examined by keeping the grid size constant and reducing the time step interval. When calculating the Courant number, the thermal velocity of electrons [94], $v_{th} = \sqrt{2k_B T_h/m_e}$, was taken as v_{max}, where T_h is the effective temperature corresponding to high energetic electrons. The effect of the Courant number on the plasma parameters is summarized in Table 5.3 and the effect on ion density, electric potential and EEDF is shown in Fig. 5.5 and Fig. 5.6. As can be seen from the results, the inconsistency is clearly seen as the number of Courant moves away from 1 as expected.

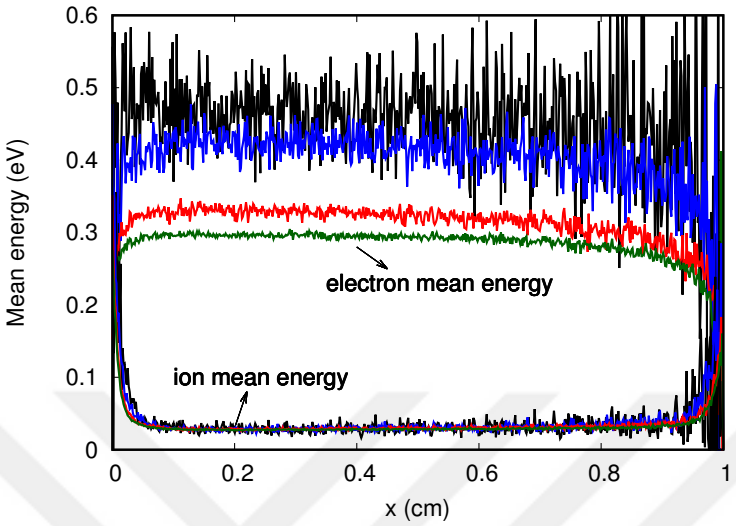


(a)

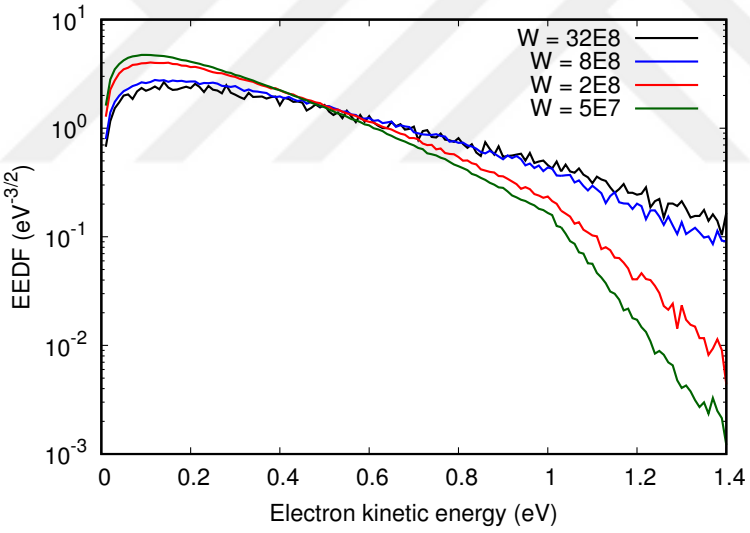


(b)

Figure 5.3: Effect of particle weighting on (a) the Na^+ ion number density and (b) the electric potential.

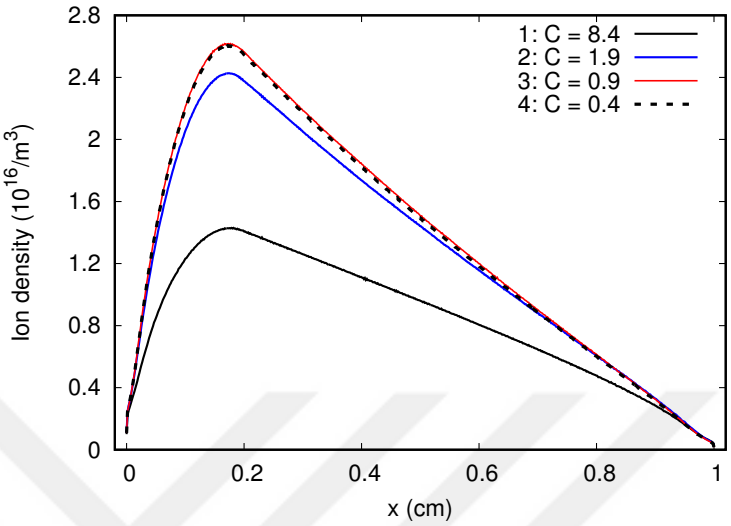


(a)

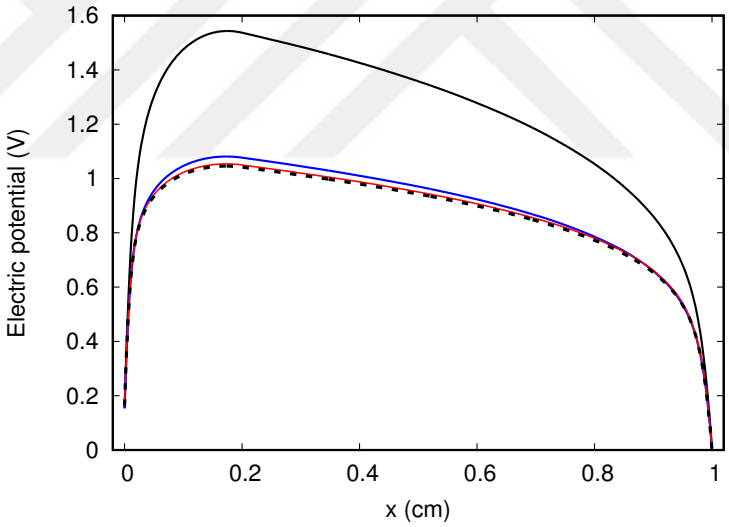


(b)

Figure 5.4: Effect of particle weighting on (a) Na^+ ion and electron mean energies and (b) the EEDF.



(a)



(b)

Figure 5.5: Effect of the Courant number on (a) Na^+ ion density and (b) the electric potential.

Table 5.3: Effect of Courant number on the total number of super electrons, the number of super electrons per Debye length, N_D, $w_{pe}\Delta t$ and $\Delta x/\lambda_D$. λ_D, N_D and w_{pe} were calculated about the local maximum of the electron density, using the effective temperature T_h corresponding to high energetic electron groups.

Courant Number	Tot. numb. of super electrons	N_D	$w_{pe}\Delta t$	$\Delta x/\lambda_D$	T_{max} (K)
8.37	1686436	12227	1.36	0.23	16118
1.87	2600553	6475	0.88	0.67	3224
0.87	2747504	6127	0.46	0.75	2803
0.43	2721060	6068	0.23	0.75	2776

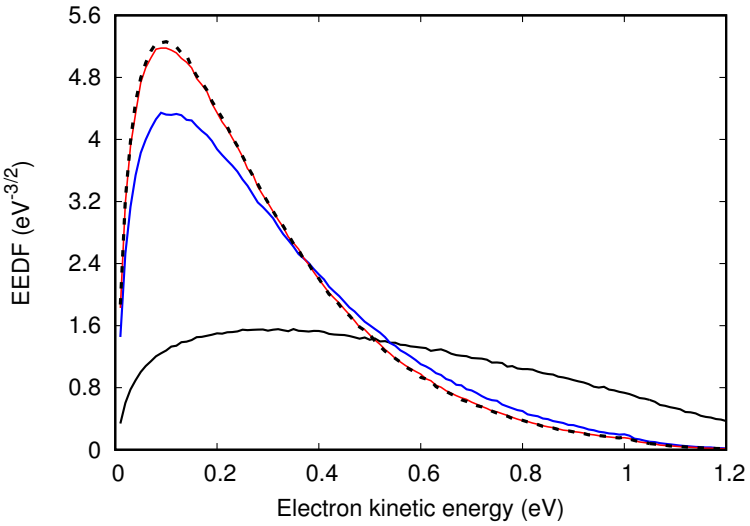


Figure 5.6: Effect of the Courant number on the EEDF.

5.4 Comparison to the Fluid Model

Numerical analysis of the photoplasma was performed using the fluid model which is explained in Section 3.1. Within this analysis, only the Penning ionization has been taken into account in the definition of the source term in the continuity equation (Eq.(3.1)). The rate coefficient for this reaction is taken as [88] $6.3 \times 10^{-9}\, cm^3/s$. The parameters used in this model are summarized in Table 5.4.

The density and electrical potential profiles obtained as a result of this analysis were added to Fig. 5.5 and Fig. 5.7. As can be seen from these figures, the results obtained from the fluid model and the PIC/MCC seem qualitatively consistent, although they show significant differences in numerical sense.

Table 5.4: The parameters used in the fluid model of photoplasma.

Species	e, Na^+
System size (cm)	1
Gas temperature (eV)	0.03
Electron temperature	0.3
μ_e (m^2/Vs)	54
μ_i (m^2/Vs)	18

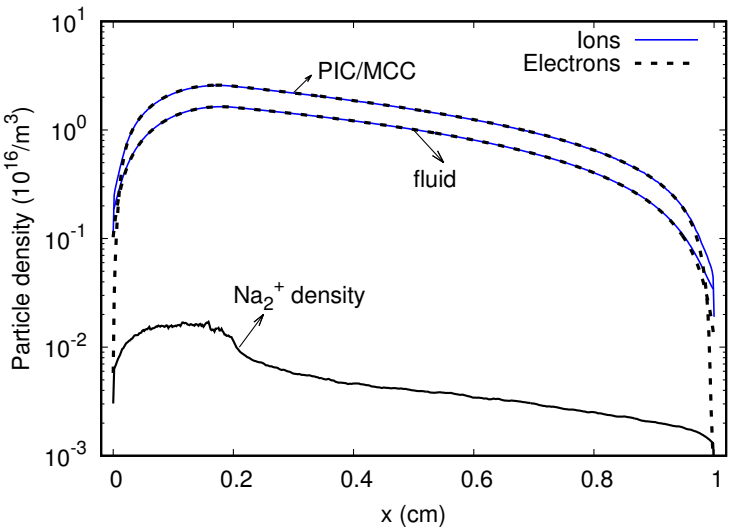


Figure 5.7: Na^+, Na_2^+ ion and electron number densities. The figure also includes the results obtained from the fluid model.

5.5 Results and Discussions

As seen in Fig. 5.7, quasineutrality is clearly visible in the interelectrode region. In addition, the difference between the sodium ion density and the molecular sodium ion density is remarkable. The reason is that the penning ionization (Eq. (5.2)) rate is much larger than the associative ionization (Eq. (5.1)) rate. In Fig. 5.3, it is seen that the plasma particles form in the range of 0-0.2 cm, where metastable atoms are present. This leads to a nonhomogeneity in the density profile and a difference in the number of particles hitting the walls. As a result, a potential difference of about 0.2 V has occurred. This potential difference supports that photoresonance plasma is a suitable tool for converting light energy into electricity.

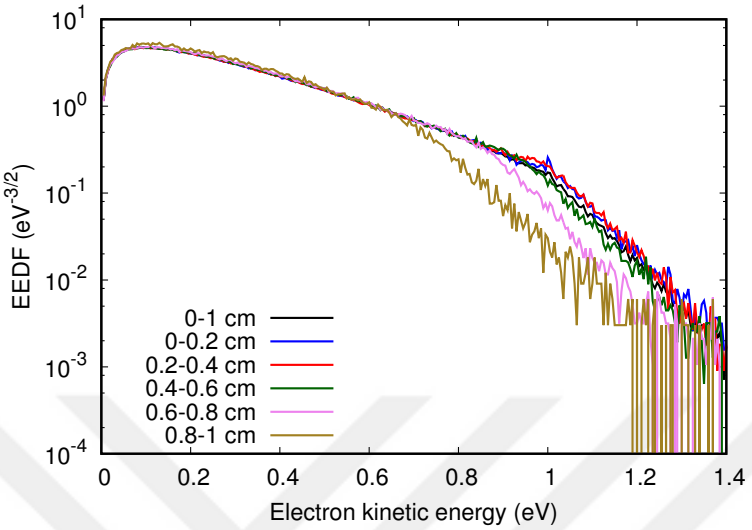
In Fig. 5.4, it is seen that the mean energy of the electrons are approximately uniform. This is because the magnitude of the electron heat conductivity is greater than the system size. The same uniformity is true for the mean energy profile of ions. The low energy observed in the ions is due to the efficient exchange of energy with the neutrals. For this reason, the energies are approximately equal to the temperature of the neutrals. For ions, uniformity in the mean energy loses its validity in regions close to walls. Because the potential drop in these regions cause the ions to accelerate.

When we look at the profile of EEDF in different regions of the discharge volume (Fig. 5.8), it can be seen that EEDF is composed of two different regions ($\varepsilon < 1eV$ and $\varepsilon > 1eV$). The first region ($\varepsilon < 1eV$) has a Maxwellian distribution and has a temperature corresponding to the mean energy of the electrons (see Fig. 5.4). It is known that 1 eV corresponds to the energy of the Penning electrons formed as a result of penning ionization of metastable sodium atoms (Eq. (5.2)). Considering the potential drop of about 1 Volt (see Fig. 5.3), it is understood that mainly Penning electrons strike the walls and are responsible for this potential drop. On the other hand, it is concluded that low-energy electrons ($\varepsilon < 1eV$) could not escape, trapped in the volume and performed elastic collisions with neutrals. Thus, they bring the first region seen in EEDF. This explains the formation of two separate regions in the graph.

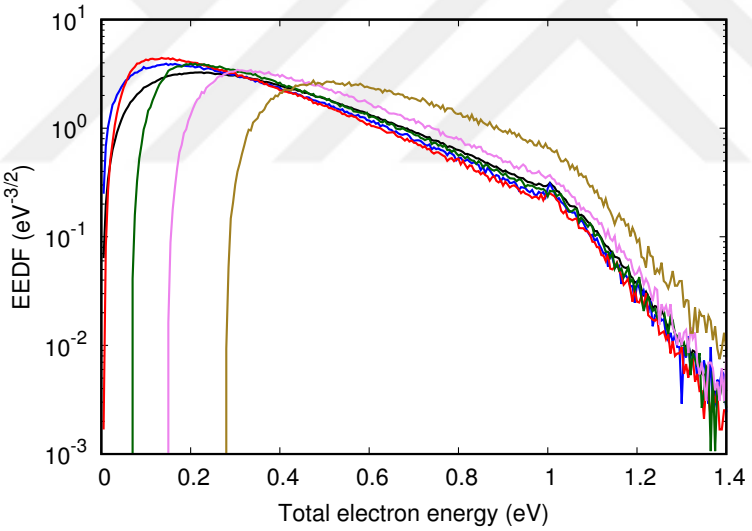
5.6 Conclusion

Parallel 1d3v PIC/MCC code was adapted to Photoresonance plasma sustained in a sodium alkali metal vapor. First of all, we investigated the effect of weighting and Courant number in order to be able to get converged results. It is assumed that the light is absorbed non-uniformly and, consequently, metastable atoms have a step-wise density distribution. Then, the basic plasma discharge parameters were examined and compared with the results obtained with the fluid model.

As a result, non-uniformity was obtained in the density distributions of the particles, and when the corresponding potential profile was examined, a potential difference of about 0.2 V was obtained. This is a result that supports the usability of the photoresonance plasma as a photoelectric converter.



(a)



(b)

Figure 5.8: The EEDF as function of the kinetic electron energy (a) and the total electron energy (b) at different regions of the discharge volume.

CHAPTER 6

SIMULATION OF THE PLES METHOD

The PLES method is an alternative to high vacuum electron spectroscopy devices. Traditional electron spectroscopy [95] explores the energy of electrons generated as a result of the ionization of impurities A by particles B^* (metastable atoms or VUV photons) with the energy ε_p to obtain information about atomic or molecular gas mixtures,

$$A + B^* \rightarrow A^+ + B + e. \tag{6.1}$$

In order for these reactions to take place, the energy of B^* must be higher than the ionization energy of A. The energy of the resulting electron is as

$$\varepsilon_e = \varepsilon_p - \varepsilon_i. \tag{6.2}$$

In this way, information about the atoms or molecules in the mixture is obtained and their concentrations are measured. Although this method is quite simple, it takes a long time to apply because of the high vacuum requirement. To get rid of these requirement, as mentioned in the Introduction, based on the PLES method, a new method has been proposed by Kolokolov et al. [17, 18] for the detection of impurities in the gas. Kudryavtsev et al. [19–22] were able to demonstrate this method experimentally and identify the impurities by examining the EEDF graph.

In order for this method to be usable, penning electrons (Eq. (1.2)) need to reach the electrodes without losing their energy. In order to achieve this, the condition which

has the form

$$\lambda_\varepsilon = \lambda/\sqrt{\delta} > 100\lambda, \tag{6.3}$$

should be satisfied. As a result of this requirement, electrons with energy $\varepsilon > e\Phi_w$ reach the electrodes while protecting their energy [96] and non-local EEDF forms. Here, λ, λ_ε, $\delta = 2m_e/M$ and Φ_w is the electron mean free path, the electron energy relaxation length, the ratio of the electron mass to the heavy particle mass and the potential drop between the discharge axis and the wall, respectively. Penning electrons in the non-local EEDF are observed as sharp peaks around ε_p energies (Eq. (1.3)). This observation was carried out in Refs. [19–22] in the study of short glow discharges in helium doped with small amount of impurity gases by analyzing the current-voltage characteristic,

$$I_e = \frac{1}{4} eS \int_{\sqrt{2eU/m}}^{\inf} v f(v) \left(1 - \frac{2eU}{mv^2}\right) dv, \tag{6.4}$$

where U is the scanning voltage and S is the cathode area.

They obtained peaks corresponding to the energies of the penning electrons in the graph of the EEDF,

$$f\left(\sqrt{2eU/m}\right) = \frac{4m}{e^2 S} U \frac{d^2 I_e}{dU^2}, \tag{6.5}$$

obtained by the second derivative of the probe current according to Druyvestein's formula (see Fig. 6.1). By examining the energies of these peaks it is possible to detect impurities.

For the development of the PLES method, optimum experimental parameters and conditions of use need to be determined. For this reason, there is a need for a simulation that can accurately express this method. However, a numerical analysis of PLES has not been done until now. The most readily available numerical technique is the Fluid model, but as mentioned in section 3.1, it is not the right choice for the simulation of the PLES method, which is a non-local plasma application. It is only

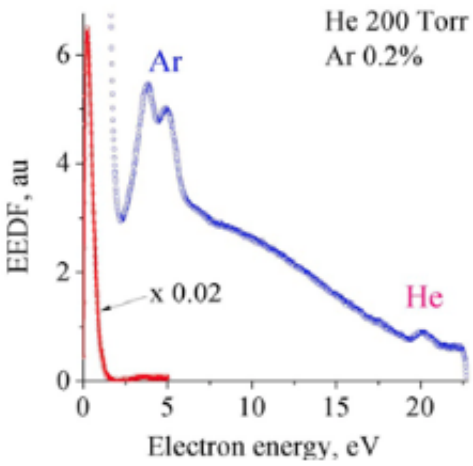


Figure 6.1: Electron energy spectra in He-Ar mixture at 11 mA discharge current, 0.9 V modulating voltage and 1 mm cathode-anode gap. *Adopted from Ref. [19].*

through a kinetic approach that the peaks corresponding to impurities can be obtained correctly.

6.1 Model

In the present work, parallel 1d3v PIC/MCC code was used to simulate dc glow discharge of helium and 0.2% argon mixture using basic experimental conditions [19–22]. The main reaction observed in the PLES is the Penning ionization reaction. The expected penning ionization reactions between the metastable helium atoms (singlet and triplet) and the argon atoms are

$$He^*(2^3S_1) + Ar(0) \rightarrow He(0) + Ar^+(^2p_{3/2}) + e_p(4.06\,eV), \tag{6.6}$$

$$He^*(2^1S_0) + Ar(0) \rightarrow He(0) + Ar^+(^2p_{3/2}) + e_p(4.85\,eV). \tag{6.7}$$

The cross-section values were taken as $5.3 \times 10^{-16}\ cm^2$ and $16.4 \times 10^{-16}\ cm^2$ for these reactions, respectively [97]. In addition to these reactions, elastic, excitation and ionization reactions between electrons and neutrals (Fig. 4.9), isotropic and backward

Table 6.1: The parameters used in the PLES simulation.

Weighting	1.6×10^8
Neutral density $(1/m^3)$	1.4×10^{23}
Voltage (V)	350
Cell number	1333
Time step (s)	2×10^{-11}
Simulation time (s)	4×10^{-5}
SEE coefficient, γ	0.15
Reflection coefficient, r	0.2

scattering reactions between ions and neutrals (Eqs. (4.21) and (4.22)) are also taken into account in this simulation.

The change over time in the densities of metastable helium atoms are investigated based on the fluid approach,

$$\frac{\partial n}{\partial t} - D\frac{\partial^2 n}{\partial x^2} = S, \tag{6.8}$$

where S is the excitation source term. Metastable helium atoms are assumed to be absorbed at the electrodes. The diffusion coefficient is calculated as [98]

$$D = (420/p) \times (T_g/0.025)^{1.5}\ cm^2 s^{-1}. \tag{6.9}$$

Here, T_g is the gas temperature in eV and p is the pressure in Torr. Parameters used in the PLES simulation are shown in Table 6.1 and the numerical values obtained as a result of this simulation are summarized in Table 6.2.

6.2 Results and Discussions

Fig. 6.2 shows the electric field and potential curves obtained for the helium-argon mixture. According to these curves, the discharges studied in Refs. [19–22] have a

Table 6.2: The numerical parameters obtained as a result of the PLES simulation. λ_D and N_D are calculated at the position where the maximum electron density is found.

Total number of superelectrons	2352847
Average number of superelectrons per grid cell	1765
Debye Length, λ_D (m)	8.73×10^{-6}
N_D	5135

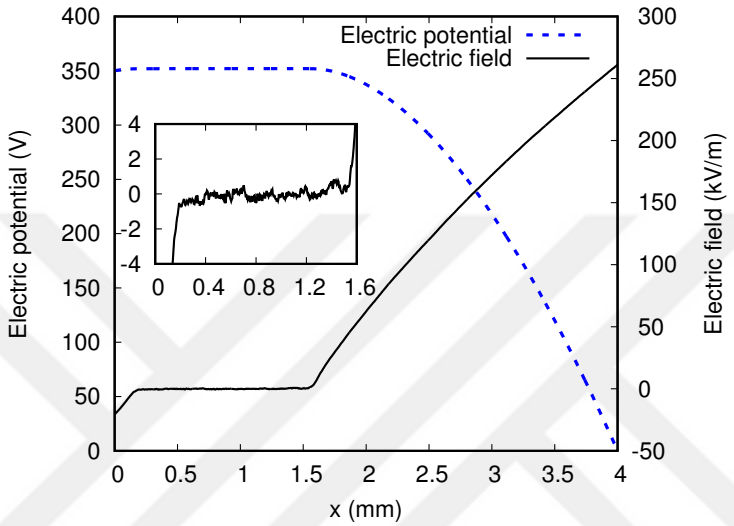


Figure 6.2: Electric field and potential profiles in the He-Ar mixture.

sheat zone of 1.8 mm in width and a negative glow zone in which low-energy electrons dominate (see Fig. 6.4). Also, in the graph, the field reversal phenomenon [99] is clearly visible in the region where the plasma density (see Fig. 6.3) is maximum.

Fig. 6.3 shows the distribution of the density of electrons and helium ions between the electrodes. As can be seen, the maximum density is about the middle of the negative glow region. According to Fig. 6.4, high energetic plasma particles appear in the cathode layer where the electric field intensity is high. In a negative glow plasma zone, the energy of the ions is close to the room temperature. The reason for this is the effective energy exchange reaction between the ions and the neutrals.

For the helium ions, when the energy distribution functions obtained at different regions between the electrodes are examined (see Fig. 6.6), there are different behaviors of ions exhibited in the plasma region and in the cathode layer. The ions in the cath-

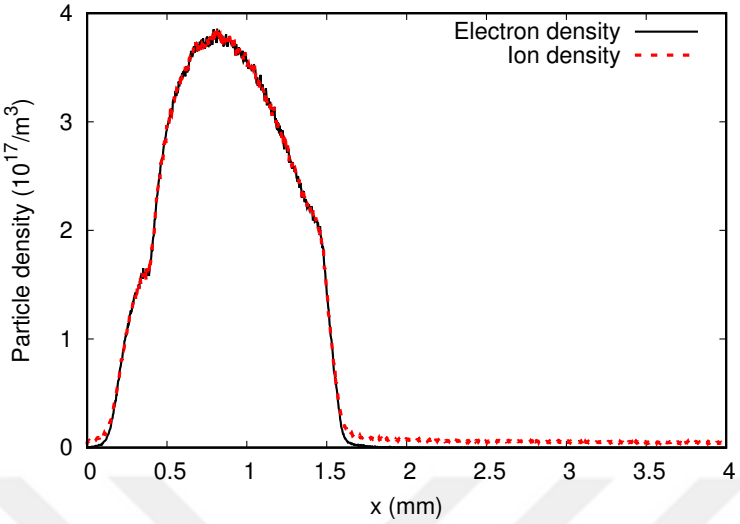


Figure 6.3: Electron and helium ion density profiles in the He-Ar mixture.

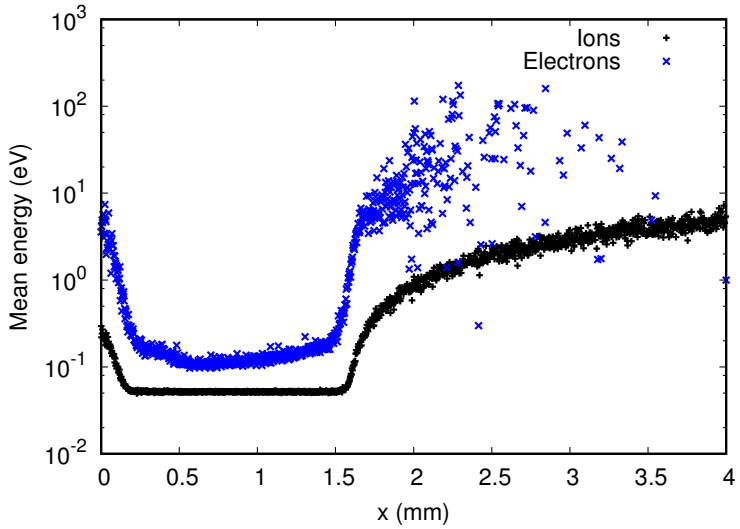


Figure 6.4: Electron and helium ion mean energies in the He-Ar mixture.

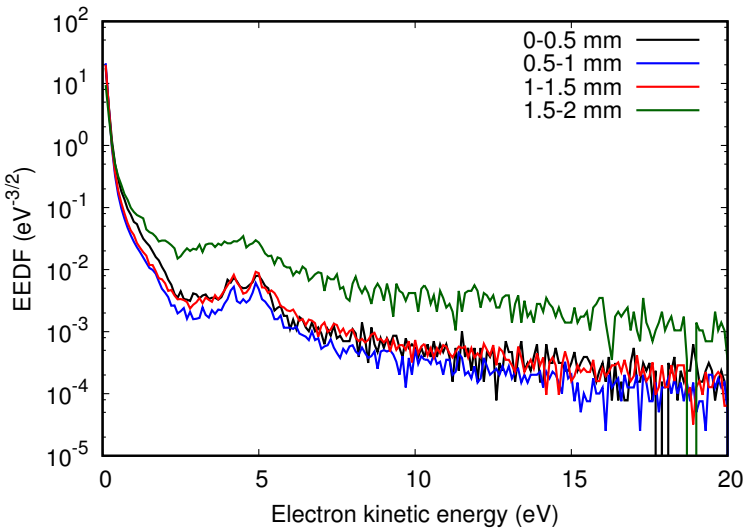


Figure 6.5: EEDF's in the He-Ar mixture.

ode layer are highly energized by the influence of the electric field while the ions in the plasma region are about at room temperature.

Finally, Fig. 6.5 shows the EEDFs of the electrons in the He-Ar mixture. As can be seen in the graph, the EEDF consists of the Maxwellian distributions of low-energy electrons and the high-energy tail due to the fast electrons. The high energy region of the graph has a continuous distribution and the peaks caused by the Penning electrons are clearly visible on this continuous distribution. The peaks are observed around 4.06 and 4.85 eV, as obtained experimentally [19]. Thus, by using these energy values obtained from the EEDF graph, the type of impurity can be clearly identified.

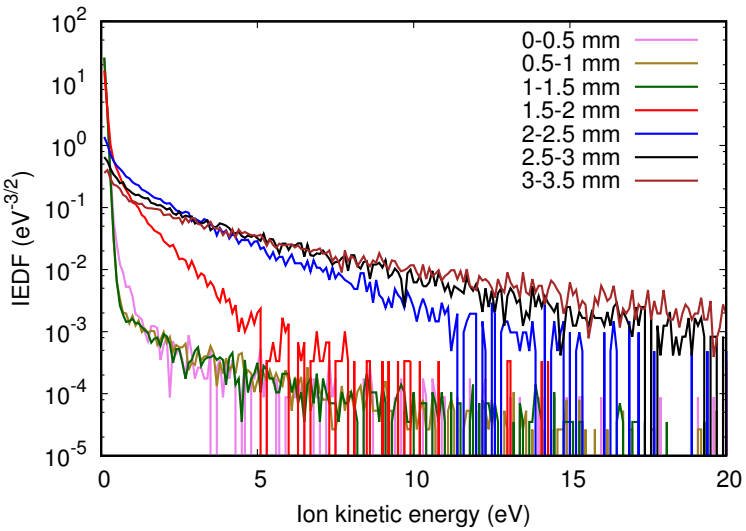


Figure 6.6: Helium ion EDF's in the He-Ar mixture.

6.3 Conclusion

Parallel 1d3v PIC/MCC simulation of DC glow discharge plasma in helium and a small amount of argon gas mixture was performed. In this simulation, the aim was to be able to observe the sharp peaks used in the detection of the impurities on the EEDF graph. In this context, the obtained EEDF graph [86] is consistent with the experimental results [19–22]. The energies of the sharp peaks (4.06 and 4.85 eV) observed in the graph correspond to the energies of Penning electrons obtained as a result of the ionization of the argon gas by the metastable helium and thus, provide the determination of the impurity argon gas.

CHAPTER 7

CONCLUSION

The 1d3v PIC/MCC code was developed to perform non-local glow discharge plasma analysis. The validity of the code was demonstrated as a result of the benchmark study [85] using RF capacitive coupled discharge conditions in helium gas [82]. Although the PIC/MCC method lead to accurate and physically adequate results, it is highly time consuming. For this reason, in order to improve the performance of the code, it was parallelized using OpenMPI and the increase in performance was examined by increasing the number of cores. As a result, an increase of 60 times in efficiency was obtained when 90 cores were used [86].

The parallel 1d3v PIC/MCC code was firstly adapted to the photoresonance plasma formed in the sodium vapor [100]. Examination of the availability of photoplasma as a photoelectric converter with a kinetic approach allows for more realistic results and thus a detailed investigation of its usability. In this context, firstly, the numerical parameters that yield converged results were determined. For this purpose, the effect of different weighting values and Courant numbers on plasma parameters was investigated. The main reaction that is responsible for the formation of the photoplasma is the Penning ionization reaction involving metastable atoms, as in the PLES method. In this simulation, it was assumed that metastable atoms have a stepwise distribution and remain constant throughout the simulation. As a result of this stepwise profile, non-uniformity was observed in the density of plasma particles. This caused a potential difference of about 0.2 volts between the electrodes. This result supports that the photoresonance plasma can be used as a photoelectric converter. In addition, the results obtained were compared with those obtained from the fluid model. Although the results obtained from two models seem consistent, they show significant numerical differences.

As another application, the parallel 1d3v PIC/MCC code was firstly adapted to the PLES method which is used to determine the impurities in the gas. There is a need for a reliable numerical model in order to develop this method and to determine the limitations of this method. For this reason, a DC glow discharge plasma simulation has been carried out for the mixture of small amount of argon gas and helium gas. In this simulation, the main purpose was to detect the electrons which are the result of the Penning ionization reaction between buffer gas and impurity. The results are consistent with experimental results [19–22], and the sharp peaks in EEDF were observed exactly at the energy values of penning electrons [86].

In future studies it is planned, first, to extend the PIC/MCC numerical code to include two spatial dimensions, and second, to increase the performance of the code by using the GPU. This will make possible to carry out simulations related to the PLES problem and the photoresonance plasma as a photoelectric converter with more realistic two-dimensional geometry, and optimization of the geometry. It is also planned to develop user friendly graphical interface that will make more convenient defining the input and output datas as well as visualization of the solutions.

REFERENCES

[1] A. Bogaerts, E. Neyts, R. Gijbels, and J. V. D. Mullen, "Gas discharge plasmas and their applications," *Spectochim. Acta B*, vol. 57, pp. 609–658, 2002.

[2] O. Buneman, "Dissipation of currents in ionized media," *Phys. Rev.*, vol. 115, pp. 503–517, 1959.

[3] J. M. Dawson, "One-dimensional plasma model," *Phys. Fluids*, vol. 5, pp. 445–459, 1962.

[4] J. M. Dawson, "Thermal relaxation in one-species, one-dimensional plasma," *Phys. Fluids*, vol. 7, pp. 419–425, 1964.

[5] C. K. Birdsall and A. B. Langdon, *Plasma Physics via Computer Simulation*. New York: McGraw-Hill, 1985.

[6] R. W. Hockney and J. W. Eastwood, *Computer Simulation Using Particles*. New York: McGraw-Hill, 1981.

[7] W. S. Lawson, "Particle simulation of bounded 1d plasma systems," *J. Comput. Phys.*, vol. 80, pp. 253–276, 1989.

[8] R. W. Boswell and I. J. Morey, "Self-consistent simulation of a parallel-plate rf discharge," *Appl. Phys. Lett.*, vol. 52, pp. 21–23, 1988.

[9] V. Vahedi and M. Surendra, "A monte carlo collision model for the particle-in-cell method: Applications to argon and oxygen discharges," *Comput. Phys. Commun.*, vol. 87, pp. 179–198, 1995.

[10] E. Kawamura, C. K. Birdsall, and V. Vahedi, "Physical and numerical methods of speeding up particle codes and paralleling as applied to rf discharges," *Plasma Sources Sci. Technol.*, vol. 9, pp. 413–428, 2000.

[11] H. R. Skullerud, "The stochastic computer simulation of ion motion in a gas subjected to a constant electric field," *J. Phys. D: Appl. Phys.*, vol. 1, pp. 1567–1569, 1968.

[12] J. J. J. Blahovec, L. A. Bowers, J. W. Luginsland, G. E. Sasser, and J. J. Watrous, "3-d ICEPIC simulations of the relativistic klystron oscillator," *IEEE Trans. Plasma Sci.*, vol. 28, pp. 821–829, 2000.

[13] P. C. Liewer and V. K. Decyk, "A general concurrent algorithm for plasma particle-in-cell simulation codes," *J. Comput. Phys.*, vol. 85, pp. 302–322, 1989.

[14] B. D. Martino, S. Briguglio, G. Vlad, and P. Sguazzero, "Parallel PIC plasma simulation through particle decomposition techniques, parallel computing," *Parallel Comput.*, vol. 27, pp. 295–314, 2001.

[15] A. B. Blagoev, Y. M. Kagan, N. B. Kolokolov, and R. I. Lyagushchenko, "Electron energy distribution in the after-glow," *Sov. Phys.-Tech. Phys.*, vol. 19, pp. 211–215, 1974.

[16] N. B. Kolokolov and P. M. Pramatarov, "Interaction between metastable atoms in a helium afterglow," *Sov. Phys.-Tech. Phys.*, vol. 23, pp. 176–177, 1978.

[17] N. B. Kolokolov, A. A. Kudrjavtsev, and A. B. Blagoev, "Interaction processes with creation of fast electrons in the low temperature plasma," *Phys. Scripta*, vol. 50, pp. 371–402, 1994.

[18] A. A. Kudryavtsev, "A New Method of Gas Analysis Using Penning-Electron Energy Spectra," in *Proceedings, International Workshop Results of Fundamental Research for Investments (IWRFRI): St. Petersburg, Russia, May 24-May 26, 1999*, p. 94, 1999.

[19] M. Stefanova, P. Pramatarov, A. Kudryavtsev, and R. Peyeva, "Energy spectra of penning electrons in non-local plasma at middle and high pressures," *J. Phys. Conf. Ser.*, vol. 514, p. 012052, 2014.

[20] A. Kudryavtsev, M. Stefanova, and P. Pramatarov, "Use of nonlocal helium microplasma for gas impurities detection by the collisional electron spectroscopy method," *Phys. Plasmas*, vol. 22, p. 103513, 2015.

[21] A. Kudryavtsev, P. Pramatarov, M. Stefanova, and N. Khromov, "Registration of gas impurities in nonlocal plasma of helium microdischarge by an additional electrode-sensor," *J. Instrum.*, vol. 7, p. P07002, 2012.

[22] A. Kudryavtsev, M. Stefanova, and P. Pramatarov, "Use of dc ar microdischarge with nonlocal plasma for identification of metal samples," *J. Appl. Phys.*, vol. 117, p. 133303, 2015.

[23] I. Beterov, A. Eletskii, and B. M. Smirnov, "Resonance radiation plasma (photoresonance plasma)," *Sov. Phys. Usp.*, vol. 31, pp. 535–554, 1988.

[24] F. Mohler and C. Boeckner, "Effects of gases on photoionization of cesium by line absorption," *J. Res. Nat. Bur. Standards*, vol. 5, pp. 399–410, 1930.

[25] N. D. Morgulis, Y. P. Korchevoi, and A. M. Przhonskii, "Formation of a cesium plasma by resonance radiation, physical properties," *Zh. Eksp. Teor. Fiz.*, vol. 53, pp. 417–422, 1968.

[26] A. N. Klyucharev and N. N. Bezuglov, *Processes of Excitation and Ionization of Atoms upon Light Absorption*. Izd-vo Leningr. un-ta, L., 1983.

[27] N. D. Morgulis and A. M. Przhonskii, "Nature of ionization in a photoresonant cesium plasma," *Zh. Eksp. Teor. Fiz.*, vol. 58, pp. 1873–1878, 1970.

[28] N. D. Morgulis and Y. P. Korchevoi, "Determination of the ionic composition of an arc-discharge plasma in cesium plasma," *Pis'ma Zh. Eksp. Teor. Fiz.*, vol. 8, pp. 313–315, 1968.

[29] J. R. Brandenberger, "Optovoltaic detection: A new probe for laser spectroscopy," *Phys. Rev. A*, vol. 36, pp. 76–80, 1987.

[30] N. A. Gorbunov and T. Stacewicz, "Photo emf observed upon the laser resonance excitation of sodium vapors," *Tech. Phys. Lett.*, vol. 26, pp. 654–655, 2000.

[31] N. A. Gorbunov and T. Stacewicz, "Observation of an electromotive force in a decaying photoresonance plasma of sodium vapors," *High Temp.*, vol. 39, pp. 623–625, 2001.

[32] C. Haddock and J. S. C. McKee, "Solar energy collection, concentration, and thermal conversion- a review," *Energ. Source.*, vol. 13, pp. 461–482, 1991.

[33] V. M. Andreev, B. A. Grilikhes, and V. D. Rumyantsev, *Photovoltaic Conversion of Concentrated Sunlight*. Wiley, New York, 1997.

[34] G. J. Dunning and A. J. Palmer, "Towards a high-temperature solar electric converter," *J. Appl. Phys.*, vol. 52, pp. 7086–7091, 1981.

[35] N. A. Gorbunov and G. Flamant, "Model of the plasma photovoltaic conversion of concentrated solar radiation: Short-circuit current and open-circuit voltage," *Plasma Chem. Plasma Process.*, vol. 35, pp. 799–817, 2015.

[36] `http://www.theo-physik.uni-kiel.de/~bonitz/si10/donko`. [Online; accessed 2017-07-07].

[37] M. A. Lieberman and A. J. Lichtenberg, *Principles of Plasma Discharges and Materials Processing*. Wiley, New York, 1994.

[38] A. Grill, *Cold Plasma in Materials Fabrication: From Fundamentals to Applications*. New York: IEEE Press, 1994.

[39] T. Hammer, "Applications of plasma technology in environmental techniques," *Contrib. Plasma Phys.*, vol. 39, pp. 441–462, 1999.

[40] W. Manheimer, L. E. Sugiyama, and T. H. Stix, *Plasma Science and the Environment*. Woodbury, NY: American Institute of Physics, 1997.

[41] D. M. Goebel and I. Katz, *Fundamental of Electric Porpulsion: Ion and Hall Thrusters*. Wiley, New Jersey, 2008.

[42] J. R. Coatan and A. M. Marsden, *Lamps and Lightning*. London: Arnold, 1997.

[43] A. Sobel, "Plasma displays," *IEEE Trans. Plasma Sci.*, vol. 19, pp. 1032–1047, 1991.

[44] J. Wilson and J. F. B. Hawkes, *Lasers: Principles and Applications*. New York: Prentice-Hall, 1987.

[45] `http://pulvinusgroup.com/Aver_Lites_Cfl_Bulb.aspx`. [Online; accessed 2017-07-04].

[46] Y. P. Raizer, *Gas Discharge Physics*. Springer-Verlag, 1991.

[47] N. S. J. Braithwaite, "Introduction to gas discharges," *Plasma Sources Sci. Technol.*, vol. 9, pp. 517–527, 2000.

[48] Y. T. Lee, M. A. Lieberman, A. J. Lichtenberg, F. Bose, H. Baltes, and R. Patrick, "Global model for high pressure electronegative radio-frequency discharges," *J. Vac. Sci. Technol.*, vol. 15, pp. 113–126, 1997.

[49] J. D. P. Passchier and W. J. Goedheer, "Relaxation phenomena after laser-induced photodetachment in electronegative rf discharges," *J. Appl. Phys.*, vol. 73, pp. 1073–1079, 1993.

[50] D. Loffhagen, F. Sigeneger, and R. Winkler, "Study of the electron kinetics in the anode region of a glow discharge by a multiterm approach and monte carlo simulations," *J. Phys. D: Appl. Phys.*, vol. 35, pp. 1768–1776, 2002.

[51] Z. Donko, K. Rozsa, and R. C. Tobin, "Monte carlo analysis of the electrons' motion in a segmented hollow cathode discharge," *J. Phys. D: Appl. Phys.*, vol. 29, pp. 105–114, 1996.

[52] M. Surendra and D. B. Graves, "Particle simulations of radio-frequency glow discharges," *IEEE Trans. Plasma Sci.*, vol. 19, pp. 144–157, 1991.

[53] Z. Donko, "Hybrid model of a rectangular hollow cathode discharge," *Phys. Rev. E*, vol. 57, pp. 7126–7137, 1998.

[54] R. K. Marcus and J. A. C. Broekart, *Glow Discharge Plasmas in Analytical Spectroscopy*. Wiley, England, 2003.

[55] V. Kolobov and R. Arslanbekov, "Deterministic boltzmann solver for electron kinetics in plasma reactors for microelectronics applications," *Microelectron. Eng.*, vol. 69, pp. 606–615, 2003.

[56] T. Makabe, *Advances in Low Temperature RF Plasmas: Basis for Process Design*. Amsterdam: Elsevier, 2002.

[57] F. F. Chen, *Introduction to Plasma Physics*. Springer, New York, 1974.

[58] S. Surzhikov and J. Shang, "Normal glow discharge in axial magnetic field," *Plasma Sources Sci. Technol.*, vol. 23, p. 54017, 2014.

[59] S. T. Surzhikov and J. S. Shang, "Two-component plasma model for two-dimensional glow discharge in magnetic field," *J. Comput. Phys.*, vol. 199, pp. 437–464, 2004.

[60] M. Sadiku, *Numerical Techniques in Electromagnetics*. Boca Raton, FL: CRC Press, 2001.

[61] L. C. Pitchford, S. V. ONeil, and J. R. J. Rumble, "Extended boltzmann analysis of electron swarm experiments," *Phys. Rev. A*, vol. 23, pp. 294–304, 1981.

[62] R. E. Rabson and K. F. Ness, "Velocity distribution function and transport coefficients of electron swarm in gases: Spherical-harmonics decomposition of boltzmann's equation," *Phys. Rev. A*, vol. 33, pp. 2068–2077, 1986.

[63] D. Loffhagen and F. Sigeneger, "Advances in boltzmann equation based modelling of discharge plasmas," *Plasma Sources Sci. Technol.*, vol. 18, p. 034006, 2009.

[64] V. Kolobov and R. Arslanbekov, "Simulation of electron kinetics in gas discharges," *IEEE Trans. Plasma Sci.*, vol. 34, pp. 895–909, 2006.

[65] K. Nanbu, "Probability theory of electron-molecule, ion-molecule, molecule-molecule, and coulomb collisions for particle modelling of materials processing plasmas and cases," *IEEE Trans. Plasma Sci.*, vol. 28, pp. 971–990, 2000.

[66] S. Longo, "Monte carlo models of electron and ion transport in non-equilibrium plasmas," *Plasma Sources Sci. Technol.*, vol. 9, pp. 468–476, 2000.

[67] T. Tajima, *Computational Plasma Physics*. Redwood city: Addison-Wesley, 1988.

[68] C. K. Birdsall, "Particle-in-cell charged-particle simulations, plus monte carlo collisions with neutral atoms, pic-mcc," *IEEE Trans. Plasma Sci.*, vol. 19, pp. 65–85, 1991.

[69] W. N. G. Hitchon, *Plasma Processes for Semiconductor Fabrication*. Cambridge: Cambridge University Press, 1999.

[70] V. Vahedi, G. DiPeso, C. K. Birdsall, M. A. Lieberman, and T. D. Rognlien, "Capacitive rf discharges modelled by particle-in-cell monte carlo simulation i: Analysis of numerical techniques," *Plasma Sources Sci. Technol.*, vol. 2, pp. 261–272, 1993.

[71] J. P. Verboncoeur, "Particle simulation of plasmas: Review and advances," *Plasma Phys. Control. Fusion*, vol. 47, pp. A231–A260, 2005.

[72] J. U. Brackbill and B. I. Cohen, *Multiple Time Scales*. New York: Academic, 1985.

[73] T. J. Sommerer and M. J. Kushner, "Numerical investigation of the kinetics and chemistry of rf glow discharge plasmas sustained in he, n2, o2, he/n2/o2, he/cf4/o2, and sih4/nh3 using a monte carlo-fluid hybrid model," *J. Appl. Phys.*, vol. 71, pp. 1654–1673, 1992.

[74] M. J. Kushner, "Modeling of microdischarge devices: Pyramidal structures," *J. Appl. Phys.*, vol. 95, pp. 846–859, 2004.

[75] J. K. Lee and C. K. Birdsall, "Velocity space ring-plasma instability, magnetized, part ii: Simulation," *Phys. Fluids*, vol. 22, pp. 1315–1322, 1979b.

[76] H. C. Kim, F. Iza, S. S. Yang, M. Radmilovic-Radjenovic, and J. K. Lee, "Particle and fluid simulations of low-temperature plasma discharges: Benchmarks and kinetic effects," *J. Phys. D: Appl. Phys.*, vol. 38, pp. R283–R301, 2005.

[77] Z. Donko, P. Hartmann, and K. Kutasi, "On the reliability of low-pressure dc glow discharge modelling," *Plasma Sources Sci. Technol.*, vol. 15, pp. 178–186, 2006.

[78] L. H. Thomas, *Elliptic Problems in Linear Difference Equations over a Network*. Watson Sci. Comput. Lab. Rept., Columbia University, New York, 1949.

[79] R. Fitzpatrick, "Computational physics." `http://farside.ph.utexas.edu/teaching/329/329.html`. [Online; accessed 2014-06-16].

[80] Z. Donko, "Particle simulation methods for studies of low-pressure plasma sources," *Plasma Sources Sci. Technol.*, vol. 20, p. 024001, 2011.

[81] `http://jilawww.colorado.edu/~avp/collision_data/electronneutral/ELECTRON.TXT`. [Online; accessed 2017-05-15].

[82] M. M. Turner, A. Derzsi, Z. Donko, D. Eremin, and S. J. K. et al., "Simulation benchmarks for low-pressure plasmas: Capacitive discharges," *Phys. Plasmas*, vol. 20, p. 013507, 2013.

[83] B. v7.1 (magboltz version 7.1). `http://www.lxcat.net`. [Online; accessed 2016-02-18].

[84] `http://jilawww.colorado.edu/~avp/collision_data/ionneutral/IONATOM.TXT`. [Online; accessed 2014-06-16].

[85] C. K. Sarikaya, I. Rafatov, and S. Cakir, "Validation of the particle in cell/-monte carlo collision numerical code for the rf discharge simulation," *BPL*, vol. 24, pp. 241004:36–47, 2016.

[86] C. K. Sarikaya, I. Rafatov, and A. A. Kudryavtsev, "Particle in cell/monte carlo collision analysis of the problem of identification of impurities in the gas by the plasma electron spectroscopy method," *Phys. Plasmas*, vol. 23, p. 063524, 2016.

[87] B. Carre, J. Bizau, D. Cubaynes, P. Dhez, D. Ederer, and et al., "Collisional ionization in a resonantly excited atomic vapor," *J. Phys. Colloques*, vol. 46 (C1), pp. 163–172, 1985.

[88] B. Carre, F. Roussel, G. Spiess, J. Bizau, P. Gerard, and F. Wuilleumier, "Resonant and off-resonance ionization of laser-excited sodium vapor," *Z. Phys. D-Atoms, Molecules and Clusters*, vol. 1, pp. 79–90, 1986.

[89] L. G. Huxley and R. W. Crompton, *The Diffusion and Drift of Electrons in Gases*. Wiley, New York, 1974.

[90] Phelps. `http://www.lxcat.net`. [Online; accessed 2016-02-07].

[91] R. Cote and A. Dalgarno, "Ultracold atom-ion collisions," *Phys. Rev. A*, vol. 62, p. 012709, 2000.

[92] J. Krasinski, T. Stacewicz, and C. R. Stroud, "The process of energy transfer between excited sodium atoms," *Opt. Commun.*, vol. 33, pp. 158–162, 1980.

[93] G. A. Sod, *Numerical Methods in Fluid Dynamics*. Cambridge: Cambridge University Press, 1985.

[94] V. Vahedi, G. DiPeso, C. K. Birdsall, M. A. Lieberman, and T. D. Rogolien, "Capacitive rf discharges modelled by particle-in-cell monte carlo simulation. i: Analysis of numerical techniques," *Plasma Sources Sci. Technol.*, vol. 2, pp. 261–272, 1993.

[95] S. Hufner, *Photoelectron Spectroscopy. Principles and Applications*. Springer, 2003.

[96] L. D. Tsendin, "Electron kinetics in non-uniform glow discharge plasmas," *Plasma Sources Sci. Technol.*, vol. 4, pp. 200–211, 1995.

[97] A. L. Schmeltekopf and F. C. Fehsenfeld, "De-excitation rate constants for helium metastable atoms with several atoms and molecules," *J. Chem. Phys.*, vol. 53, pp. 3173–3177, 1970.

[98] Q. Wang, D. J. Economou, and V. M. Donnelly, "Simulation of a direct current microplasma discharge in helium at atmospheric pressure," *J. Appl. Phys.*, vol. 100, p. 023301, 2006.

[99] J. P. Boeuf and L. C. Pitchford, "Field reversal in the negative glow of a dc glow discharge," *J. Phys. D: Appl. Phys.*, vol. 28, pp. 2083–2088, 1995.

[100] C. K. Sarikaya, I. Rafatov, and A. A. Kudryavtsev, “PIC/MCC analysis of a photoresonance plasma sustained in a sodium vapor,” *Phys. Plasmas*, vol. 24, p. 083505, 2017.

CURRICULUM VITAE

PERSONAL INFORMATION

Surname, Name: Kuşoğlu Sarıkaya, Cemre
Nationality: Turkish (TC)
Date and Place of Birth: 05.03.1988, Antakya
Marital Status: Married (2010)
Phone: 0 505 7438241
Fax: 0 312 2105099
email: ckusoglu@metu.edu.tr

EDUCATION

Degree	Institution	Year of Graduation
M.S.	Department of Physics, METU	2011
B.S.	Department of Physics, Gazi University	2008
High School	Merkez Lisesi, Antakya	2004

WORK EXPERIENCE

Year	Place	Enrollment
2011-2017	Departmant of Physics, METU	Research Assistant

HONORS, AWARDS AND FELLOWSHIPS

1. TÜBİTAK (The Scientific and Technology Research Counsil of Turkey), Graduate Scholarship, 2010.

2. Gazi University, Outstanding Success Award, 2008.

3. Gazi University, Certificate of High Honour, 2008.

FOREIGN LANGUAGES

Advanced English

PUBLICATIONS

Proceedings Presented in National/International Meetings

1. C. Kusoglu Sarikaya, I. Rafatov and A. A. Kudryavtsev, Particle in Cell/Monte Carlo Collision Analysis of the Problem of Identification of Impurities in Gas within the Plasma Electron Spectroscopy Method, 69th Annual Gaseous Electronics Conference (GEC), October 10-14 2016 Bochum, Germany (oral presentation).

2. C. Kusoglu Sarikaya, I. Rafatov, Validation and Parallelization of the Particle in Cell/Monte Carlo Collision Numerical Code for the RF Discharge Simulations, 9th International Physics Conference of the Balkan Physical Union, August 24-27 2015 Istanbul, Turkey (oral presentation).

3. C. Kusoglu Sarikaya, I. Rafatov, and S. Cakir, Validation of the Particle in Cell/Monte Carlo Collision Numerical Code for the RF Discharge Simulations, Turkish Physical Society 31th International Physics Congress, July 21-24 2014 Bodrum, Turkey (oral presentation).

National/International Journal Publications

1. C. Kusoglu Sarikaya, I. Rafatov and A. A. Kudryavtsev, "PIC/MCC Analysis of a Photoresonance Plasma Sustained in a Sodium Vapor", *Physics of Plasmas*, 24, 083505:1-6, 2017.

2. C. Kusoglu Sarikaya, I. Rafatov and A. A. Kudryavtsev, "Particle in cell/Monte

Carlo collision analysis of the problem of identification of impurities in the gas by the plasma electron spectroscopy method", *Physics of Plasmas*, 23, 063524:1-7, 2016.

3. C. Kusoglu Sarikaya, I. Rafatov and S. Cakir, "Validation of the Particle in Cell/Monte Carlo Collision Numerical Code fort he RF Discharge Simulation", *Balkan Physics Letters*, 24, 36-47, 2016.

4. H. Yurtseven, C. Kusoglu Sarikaya, "Investigation of the Ferroelectric Paraelectric Phase Transition in Bulk and Confined Sodium Nitrite", *Ferroelectrics*, 467, 42-49, 2014.

5. C. Kusoglu Sarikaya, H. Yurtseven, "Temperature Dependence of the Spontaneous Polarization Near the Ferroelectric-Paraelectric Transition in $NaNO_2$", *High Temperature Materials and Processes*, 32, 77-81, 2013.

PROJECTS

TUBITAK-RFBR (Russian Foundation for Basic Research) Joint Research Project 212T164, "Physical principles of control of characteristics of gas discharge with non-local plasma", 2013-2015 (Turkish project scholarship holder).